



**HAL**  
open science

## **N<sub>2</sub>-H<sub>2</sub> capacitively coupled radio-frequency discharges at low pressure. Part I. Experimental results: effect of the H<sub>2</sub> amount on electrons, positive ions and ammonia formation.**

Audrey Chatain, Miguel Jiménez-Redondo, Ludovic Vettier, Olivier Guaitella, Nathalie Carrasco, Luis Lemos Alves, Luis Silvino Alves Marques, Guy Cernogora

### ► To cite this version:

Audrey Chatain, Miguel Jiménez-Redondo, Ludovic Vettier, Olivier Guaitella, Nathalie Carrasco, et al.. N<sub>2</sub>-H<sub>2</sub> capacitively coupled radio-frequency discharges at low pressure. Part I. Experimental results: effect of the H<sub>2</sub> amount on electrons, positive ions and ammonia formation.. Plasma Sources Science and Technology, 2020, 29 (8), pp.085019. 10.1088/1361-6595/ab9b1a . insu-02867248

**HAL Id: insu-02867248**

**<https://insu.hal.science/insu-02867248>**

Submitted on 15 Nov 2020

**HAL** is a multi-disciplinary open access archive for the deposit and dissemination of scientific research documents, whether they are published or not. The documents may come from teaching and research institutions in France or abroad, or from public or private research centers.

L'archive ouverte pluridisciplinaire **HAL**, est destinée au dépôt et à la diffusion de documents scientifiques de niveau recherche, publiés ou non, émanant des établissements d'enseignement et de recherche français ou étrangers, des laboratoires publics ou privés.

# **N<sub>2</sub>-H<sub>2</sub> capacitively coupled radio-frequency discharges at low pressure. Part I. Experimental results: effect of the H<sub>2</sub> amount on electrons, positive ions and ammonia formation.**

**Audrey Chatain<sup>\*1,2</sup>, Miguel Jiménez-Redondo<sup>3,4</sup>, Ludovic Vettier<sup>1</sup>, Olivier Guaitella<sup>2</sup>, Nathalie Carrasco<sup>1</sup>, Luis Lemos Alves<sup>5</sup>, Luis Marques<sup>3</sup>, Guy Cernogora<sup>1</sup>**

<sup>1</sup>LATMOS/IPSL, UVSQ Université Paris-Saclay, Sorbonne Université, CNRS, 78280 Guyancourt, France

<sup>2</sup>LPP, École Polytechnique, Sorbonne Université, université Paris-sud, CNRS, 91128, Palaiseau, France

<sup>3</sup>Centro de Física das Universidades do Minho e do Porto, Universidade do Minho, 4710-057, Braga, Portugal

<sup>4</sup>Present address: Instituto de Estructura de la Materia, IEM-CSIC, Serrano 123, 28006 Madrid, Spain

<sup>5</sup>Instituto de Plasmas e Fusão Nuclear, Instituto Superior Técnico, Univ. Técnica de Lisboa, Lisboa, Portugal

\*e-mail: [audrey.chatain@latmos.ipsl.fr](mailto:audrey.chatain@latmos.ipsl.fr)

## **Abstract**

---

The mixing of N<sub>2</sub> with H<sub>2</sub> leads to very different plasmas from pure N<sub>2</sub> and H<sub>2</sub> plasma discharges. Numerous issues are therefore raised involving the processes leading to ammonia (NH<sub>3</sub>) formation.

The aim of this work is to better characterize capacitively-coupled radiofrequency plasma discharges in N<sub>2</sub> with few percents of H<sub>2</sub> (up to 5%), at low pressure (0.3 to 1 mbar) and low coupled power (3 to 13 W). Both experimental measurements and numerical simulations are performed. For clarity, we separated the results in two complementary parts. The actual one (first part), presents the details on the experimental measurements, while the second focuses on the simulation, a hybrid model combining a 2D fluid module and a 0D kinetic module.

Electron density is measured by a resonant cavity method. It varies from 0.4 to 5.10<sup>9</sup> cm<sup>-3</sup>, corresponding to ionization degrees from 2.10<sup>-8</sup> to 4.10<sup>-7</sup>. Ammonia density is quantified by combining IR absorption and mass spectrometry. It increases linearly with the amount of H<sub>2</sub> (up to 3.10<sup>13</sup> cm<sup>-3</sup> at 5% H<sub>2</sub>). On the contrary, it is constant with pressure, which suggests the dominance of surface processes on the formation of ammonia. Positive ions are measured by mass spectrometry. Nitrogen-bearing ions are hydrogenated by the injection of H<sub>2</sub>, N<sub>2</sub>H<sup>+</sup> being the major ion as soon as the amount of H<sub>2</sub> is > 1%. The increase of pressure leads to an increase of secondary ions formed by ion/radical – neutral collisions (ex: N<sub>2</sub>H<sup>+</sup>, NH<sub>4</sub><sup>+</sup>, H<sub>3</sub><sup>+</sup>), while an increase of the coupled power favors ions formed by direct ionization (ex: N<sub>2</sub><sup>+</sup>, NH<sub>3</sub><sup>+</sup>, H<sub>2</sub><sup>+</sup>).

**Keywords:** cold plasma, CCP discharge, N<sub>2</sub> H<sub>2</sub> mixture, NH<sub>3</sub>, IR absorption, neutral and ions mass spectrometry, plasma surface interactions.

## 1. Introduction

---

Nitrogen and hydrogen are usual gases, and a lot of studies have been conducted with the objective to understand pure N<sub>2</sub> [1,2] and pure H<sub>2</sub> [3,4] plasmas. However, as soon as the two gases are mixed, plasmas become different, and much harder to understand. Today questionings deal with the chemical mechanisms happening in the gas phase and on the surfaces in contact, and especially with the processes leading to the formation of ammonia (NH<sub>3</sub>).

Many technological applications use N<sub>2</sub>-H<sub>2</sub> plasmas nowadays, as the plasma species formed with both hydrogen and nitrogen have interesting properties. A major issue is the industry of thin film growth, among which are the silicon (SiN) films fundamental for the semiconductor and the photovoltaic industries. These films are formed by plasma-enhanced chemical vapour deposition (PECVD), with gas mixtures containing Si, N<sub>2</sub> and H<sub>2</sub> [5–8]. Another major industrial application of N<sub>2</sub>-H<sub>2</sub> plasmas is nitriding, used to harden metal surfaces [9,10]. In nuclear fusion, N<sub>2</sub> is added to hydrogen plasma to inhibit organic film deposition on walls [11–13]. The formation of ammonia has a strong industrial interest as ammonia is already produced in huge quantities to be used as a basic precursor for the synthesis of chemicals such as fertilizers. The current technique known as the Haber-Bosch process has a yield of 15-20% and research is on-going to exceed this yield using plasmas [14]. In aerospace applications, N<sub>2</sub>-H<sub>2</sub> plasmas are used for propulsion through arcjet thrusters [15]. In all these applications, the understanding of N<sub>2</sub>-H<sub>2</sub> plasma is fundamental to optimize the protocols and designs of technologies.

The understanding of N<sub>2</sub>-H<sub>2</sub> plasmas is not only considered for in the industrial world, but also in astrophysics and planetary sciences. In the interstellar medium for instance, nitrogen and hydrogen excited species and ions are present in large quantity. A current issue is to understand the formation processes of ammonia which abundance is not explained by current models. [16–18] explain it could be due to an additional surface chemistry on ice and dust particles. Another issue is about the detection of N<sub>2</sub> in radio astronomy. N<sub>2</sub> has no rotational transitions and is therefore not detectable. However, N<sub>2</sub>H<sup>+</sup> can be detected. To deduce the density of N<sub>2</sub> from measurements on N<sub>2</sub>H<sup>+</sup> requires a complete understanding of the sources and sinks of N<sub>2</sub>H<sup>+</sup> in this environment [19,20]. The study of the ionospheres of planets also often deals with N<sub>2</sub>-H<sub>2</sub> plasmas. Among them, the ionosphere of Titan, the largest moon of Saturn, is of major interest as it is the place of formation of very complex organic aerosols. Titan's ionosphere is mainly composed of ~97.6% of N<sub>2</sub>, ~2% of CH<sub>4</sub> and ~0.4% of H<sub>2</sub> [21]. To understand the complex ion chemistry happening there, different groups simulate the ionosphere of Titan with laboratory cold plasmas, with for instance a radiofrequency capacitively coupled plasma (RF CCP) discharge [22], a pulsed discharge nozzle (PDN) freejet planar expansion [23] or a DC glow discharge [24]. In such plasmas, nitrogen and hydrogen are massively present, and it is necessary to understand their behavior in a simplified N<sub>2</sub>-H<sub>2</sub> discharge before adding CH<sub>4</sub> to the mixture. In particular, NH<sub>3</sub> and NH<sub>4</sub><sup>+</sup> are present in Titan's upper atmosphere [21,25] but current models deriving NH<sub>3</sub> amounts from NH<sub>4</sub><sup>+</sup> measurements underestimate NH<sub>3</sub> production by a factor of 10-100 [26]. The possible production of NH<sub>3</sub> on surfaces (like on solid aerosols) is still to be investigated.

The study of plasmas requires experiments and numerical simulations to closely work together. Diagnosis and modelling of N<sub>2</sub>-H<sub>2</sub> discharges started with the works of [27,28] on DC glow discharges. [29,30] continued this work with the complexification of the chemical model, especially with the introduction of surface kinetics. Ammonia density among other species could not be explained by bulk processes, and led [30] to discover the fundamental role of surface reactions on the global discharge kinetics. They also showed that surface kinetics is highly dependent on the surface state: the surface material, but also the way it has been processed before the measurements. The complex ion processes are studied in [16,17,31] working at low pressure (0.8-8 Pa), while details of mechanism at the surface are described in [14,32] working at atmospheric pressure.

Plasma characteristics depend on the geometry and on the nature of the discharge. All the studies cited above have been performed in DC glow discharges, which are very homogeneous and can be modelled in 0D.

However,  $N_2$ - $H_2$  plasma applications cited above do not all work in DC glow discharges. In particular, material processing or functionalization is often performed with radiofrequency capacitively coupled (RF CCP) discharges [10,33], as well as the study of Titan's ionosphere in [22]. Some first studies addressed microwave discharges [34] and radiofrequency inductively coupled plasmas [35]. However, to our knowledge, none of them deals with RF CCP discharges.

RF CCP discharges are more complex to diagnose and to model than DC plasmas. Indeed, charged species are not homogeneously distributed in the plasma. For that purpose, [36,37] implemented a two-dimensional model to describe pure  $H_2$  RF CCP discharges. It is a hybrid model in which the dynamics of charged species are described by a 2D, time-dependent fluid module, while a zero-dimensional kinetic module solves the chemistry. This work has been continued for pure nitrogen in [38].

Experiments and models in glow DC discharges (references cited above) show the strong modifications of pure  $N_2$  (and pure  $H_2$ ) plasmas with the small addition of  $H_2$  (resp.  $N_2$ ), and the major effect of surface processes on the plasma global kinetics.

Our objective here is to analyze such modifications in capacitively coupled radio-frequency discharges by the addition of small amounts of  $H_2$  (up to 5%) in an initially pure  $N_2$  plasma, at low pressure (0.3 – 1 mbar) and low power (3 – 13 W) conditions.

Different measurements are performed, probing electric parameters, electron density, ammonia density and positive ion evolutions. These measurements have then been used to improve the model previously adapted for pure  $N_2$  discharges [38], the main additions being the new  $N_xH_y$  species, their gas-phase reactions and the surface processes. For clarity, we divided the work in two parts: paper I (this one) focusing on experimental measurements and paper II describing the numerical simulation and the comparison with the experimental data.

## 2. Experimental setup

### 2.1 A RF CCP discharge in $N_2$ - $H_2$

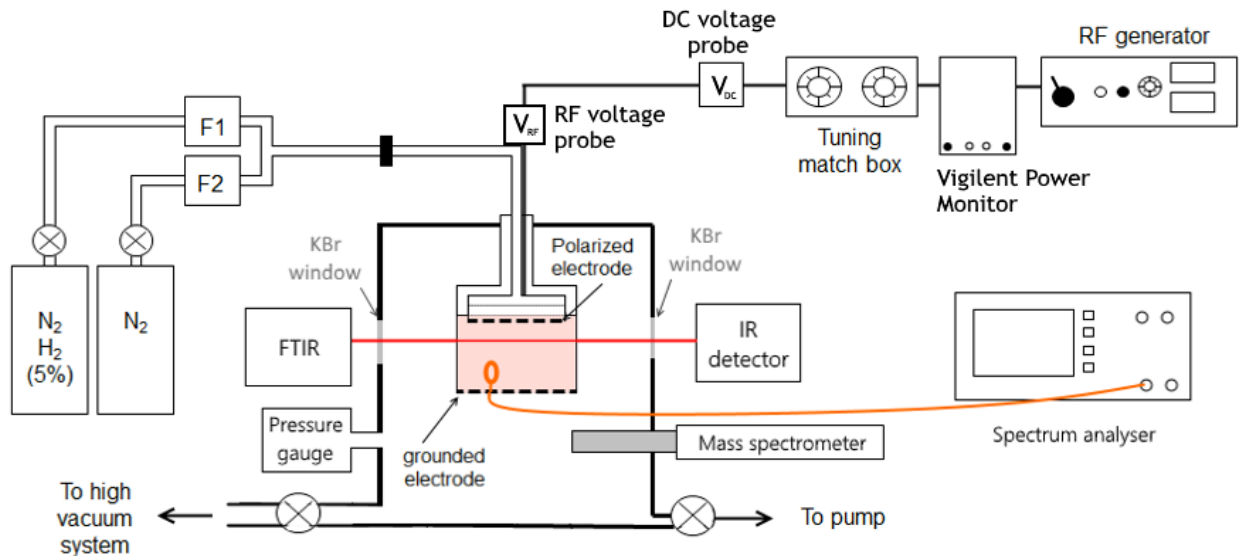


**Figure 1.** Experimental set up.

The experiment is a radiofrequency capacitively coupled plasma discharge (RF CCP) set up presented in figure 1 [22,39]. It is a wide stainless steel cylindrical chamber, with a diameter of 30 cm and a height of 40 cm. Two KBr windows are disposed for IR absorption measurements. In the middle of the chamber, the RF voltage is applied to the upper electrode which is a stainless steel disk grid of 12.6 cm in diameter. Through this grid the gas is injected as a homogeneous flow. The plasma is confined in a grounded aluminum alloy cylindrical box surrounding the upper electrode. The bottom of the box at 3.4 cm from the upper electrode is also a grid to let the gas go through. Four 2 cm-large and 4 cm-high slits are pierced in the sides of the box for the instruments to access the plasma. There are covered by thin metallic grids when unused in order to maintain the plasma in the box.

Some parameters are varied for this study: the percentage of H<sub>2</sub>, the total pressure and the injected RF power. Before each experiment the chamber is heated and pumped to high vacuum (down to 10<sup>-6</sup> mbar) with a turbomolecular pump in order to clean the chamber. At the beginning of each experiment, the selected gas mixture is injected in continuous flow. The gas flow stabilizes after ~3 min and only then the plasma is ignited.

High purity gases (Air Liquide N60 Alphagaz 2, purity > 99.999%) are used. The amount of H<sub>2</sub> from 0 to 5% is obtained by mixing pure N<sub>2</sub> and a 95% N<sub>2</sub> - 5% H<sub>2</sub> mixture. The mixing is obtained by two mass flow controllers (MKS 100 Standard Cubic Centimeter per Minute (sccm), full scale accuracy 1%) injecting gas with individual flow varying from 2 to 70 sccm, and giving a global gas flow from 10 to 70 sccm. Pressure, measured by a capacitance gauge (MKS baratron 100 mbar full scale accuracy 0.15%), can therefore be adjusted from 0.3 to 1 mbar. The RF power generator delivers an incident power of 5 to 30 W at 13.56 MHz (SAIREM GRP01KE – 100 W maximum power). A matchbox is connected between the generator and the plasma for impedance adaptation.

## 2.2 Electrical measurements

The RF peak-to-peak voltage ( $V_{RF,pp}$ ) is one of the key reference parameters used to describe the experimental conditions. It is measured by a high-voltage probe connected to the driven electrode by a stainless steel tube of 30 cm in length, which induces almost no potential drop. It is positioned under vacuum to avoid electrical breakdown. A DC voltage probe situated between the polarized electrode and the match box gives the self-bias potential  $V_{DC}$  with a precision of 0.3V. The self-bias potential appears when both electrodes differ in size and when a coupling capacitor is present between the RF power supply and the electrode (the match box in figure 1). In these conditions, the asymmetry of currents collected on the two electrodes creates the self-bias potential [40]. It is related to the electron density and the electron temperature.

RF power measurements are performed by a digital V-I probe (Vigilant Power Monitor Solayl) positioned between the generator and the match box. It gives the transmitted power with an accuracy of 2%. The incident and reflected power and the RF current ( $\pm 0.01A$ ) are measured. The transmitted power measured with plasma ON is subtracted by the transmitted power with plasma OFF for the same RF peak-to-peak voltage to obtain the power absorbed by the plasma.

## 2.3 Electron density measured by a resonant cavity method

One of the most relevant parameter of the plasma is the electron density. It is determined in various sets of parameters thanks to a resonant cavity method, as similarly done in [38,39,41].

The metallic confining box is used as a microwave resonance cavity. Microwaves are emitted and measured by an antenna loop of 0.8 cm in diameter. The antenna is positioned perpendicularly to a box radius to enhance the transversal modes (TM). A second loop can be positioned symmetrically to measure the transmitted signal. Measurements done in transmission with two antennas and in reflexion with only one antenna have been

compared (see appendix A1). We found that reflexion measurements are more precise, so this mode was chosen in the following. Microwaves from 1 to 4 GHz are delivered and detected with a spectrum analyzer (Rohde & Schwarz ZVL Accuracy of reflection measurements: < 0.4 dB for 0 dB to -15 dB and < 1dB for -15 dB to -25 dB).

Microwaves emitted in a metallic cylindrical box ( $R_c = 6.9$  cm,  $L_c = 3.5$  cm) theoretically lead to resonant  $TM_{l,m,p}$  modes described by:

$$f_{lmp} = \frac{c}{2\pi\sqrt{\epsilon_r}} \sqrt{\frac{\lambda_{lm}^2}{R_c^2} + \frac{p^2\pi^2}{L_c^2}} \quad l, p = 0, 1, 2 \dots \quad m = 1, 2 \dots \quad (1)$$

where  $\lambda_{lm}$  is the  $m^{\text{th}}$  zero of the equation  $J_l(\lambda)=0$ , where  $J_l$  is the  $l^{\text{th}}$  Bessel function. In air or vacuum, the theoretical resonant frequencies lower than 4 GHz are the transversal modes  $TM_{010}$  (1.66 GHz),  $TM_{110}$  (2.65 GHz) and  $TM_{210}$  (3.55 GHz).

The dielectric constant  $\epsilon_r$  of the plasma is a function of the electron density. It induces a shift in the resonance frequency with and without plasma, which gives the relation: [42]

$$n_e = A \times \frac{8\pi^2 m_e \epsilon_0}{e^2} \times \frac{f^2}{f_0} \times (f - f_0) \quad (2)$$

where  $n_e$ ,  $m_e$  and  $e$  are respectively the electron density, mass and charge,  $f$  and  $f_0$  the resonant frequencies respectively with and without plasma. Finally,  $A$  is a factor depending on the cavity geometry and the chosen mode [38]. It was calculated for pure  $N_2$  plasmas taking into account  $n_e$  profiles in our conditions: 1.03 for  $TM_{010}$ , 1.09 for  $TM_{110}$  and 1.14 for  $TM_{210}$  (G. Wattiaux – private communication).

Improvements have been done on the technique since [38,39,41]. Microwave resonance spectra directly acquired in the confining box show parasitic absorption. These absorptions are attributed to the gap between the polarized electrode and the grounded box. We added a thin copper crown in between the polarized electrode and the box sides in order to create a more ideal cylindrical cavity. Parasitic absorption peaks disappear with this method (see appendix A1). Figure 2 shows a scheme of the addition of the copper crown in the experiment, and the resonance shifts obtained for a  $N_2 H_2$  (95-5) mixture at 0.9 mbar.

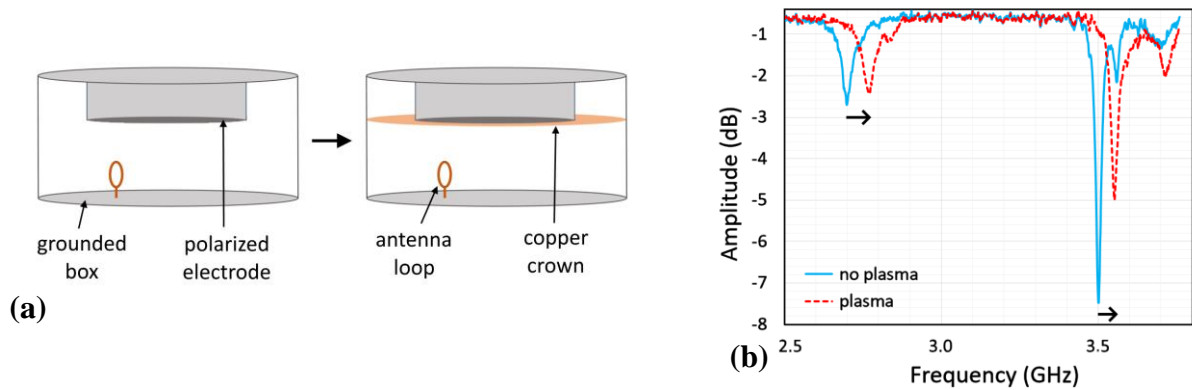


**Figure 2.** Electron density measurement. (a) Scheme of the installation of a copper crown between the polarized electrode and the confining grounded box to improve the signal. (b) Spectra showing the resonant frequencies in the box, before and after plasma ignition (0.91 mbar –  $N_2$ - $H_2$  5% - 13.5 W)

Two peaks are especially visible at 2.70 and 3.50 GHz, attributed to the modes  $TM_{110}$  and  $TM_{210}$ . Measurements with both frequencies give similar results for the electron density, with differences of only 2%. Therefore, we then focused only on the  $TM_{210}$  mode because it had a greater intensity. The resolution of frequency measurements is  $\sim 0.5$  MHz, which gives a resolution of  $\sim 6.10^7$   $cm^{-3}$  for electron density.

We observe a slow shift of the resonance when the plasma is turned OFF due to the box cooling, changing slightly its dimensions and therefore the resonance frequency. Consequently,  $f_0$  is measured just after plasma

extinction for all the experimental conditions. Each measurement was done at least 2 to 3 times on different days to ensure the repeatability. For measurements with identical  $H_2$  amount, pressure and RF peak-to-peak voltage, the mean standard deviations are  $\sim 8\%$  for the electron density,  $\sim 5\%$  for the transmitted power and  $\sim 2\%$  for the DC voltage.

## 2.4 Ammonia by IR transmission spectroscopy and neutral mass spectrometry

### 2.4.1 Quantification of ammonia density by IR transmission spectroscopy

Simple gaseous molecules have previously been studied in PAMPRE using IR spectroscopy. The plasma was ignited during hours and molecules accumulated in an external [43] or internal [44] cold trap. Thereafter, the content of the trap was released in the chamber for the IR analysis. The main objective was to obtain densities high enough for an accurate IR measurement. This method was tested for ammonia but without a good accuracy because ammonia adsorbs easily on metallic surfaces. Therefore, direct measurements during the plasma are necessary. Even if ammonia is homogeneously distributed in the chamber (see appendix A2), its density is low and the absorption length between the two KBr windows (50.8 cm) is not long enough to easily measure the absorption. The parameters of the FTIR spectrometer have to be finely adjusted to maximize the signal. We focused on a short wavelength range centered on the two most intense  $NH_3$  IR absorption bands (between 850 and 1050  $cm^{-1}$ ).

Spectra are taken by a Fourier Transform IR spectrometer (FTIR – Nicolet 6700 from Thermo Fisher), with a MCT detector and a Michelson speed of 0.63 cm/s. 3000 to 6000 scans are accumulated, at resolutions between 1 and 4  $cm^{-1}$ . A single final spectrum takes 2 to 3 hours to be obtained. The IR analysis is used for calibration of the MS (see part 2.4.2 and appendix A2).

Final spectra are analyzed with a program developed by [45]. It deduces the ammonia amount from the IR absorption spectrum, the experimental conditions (mainly total pressure) and the molecular data from the HITRAN database. The main uncertainty on the deduced value of ammonia density is the neutral gas temperature which requires a higher resolution to be deduced from the IR spectra. A Resistance Temperature Detector (RTD, PT 100) measures the polarized electrode temperature. This temperature increases from 25 to 60°C during the 3-hours plasma duration. Such gas temperature variations lead to 15-20% uncertainty on the ammonia density calculation. Figure 3 presents a typical IR absorption spectra recorded for a plasma of 3% of  $H_2$  at 0.53 mbar.

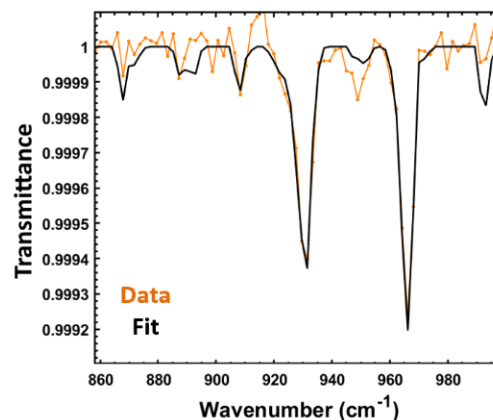


**Figure 3.** IR spectra of ammonia detected in the experiment ( $N_2$ - $H_2$  3% - 0.53 mbar – 8.4 W) and fitted to deduce ammonia density. Spectra integrated over 1h45 at 4  $cm^{-1}$  resolution.

Eight spectra were acquired for different conditions: for amounts of  $H_2$  of 1, 3 and 5% and at two different pressures, 0.53 mbar and 0.91 mbar.

#### 2.4.2 Calibration of the mass spectrometer with simultaneous IR spectroscopy measurements

The ammonia amount is measured in the chamber by a quadrupole mass spectrometer (MS – Hiden Analytical, Electrostatic Quadrupole Plasma (EQP) series). The movable grounded sampling stick is positioned at a few centimeters from the confining box, with a sampling orifice of 100  $\mu\text{m}$ . Ammonia is detected with the residual gas analyzer mode (RGA), with an electron energy of 70 V and a filament intensity of 5  $\mu\text{A}$ . The detector is a Secondary Electron Multiplier (SEM). Spectra were acquired with  $m/z$  ratio from 2 to 60, averaged on 3 to 10 scans, with a total acquisition time of 1-2 minutes, and a dynamic range of  $10^6$  c/s.

Ammonia fragmentation main ion peaks in RGA are at  $m/z$  17 and 16. Traces of water are detected at  $m/z$  18. We deduced from the peak at  $m/z$  18 and the NIST database the minor contributions of water to the peaks at  $m/z$  17 and 16 and removed it to obtain the contribution of ammonia (5-20% correction). Figure 4 presents mass spectra recorded for 3 gas mixture conditions.

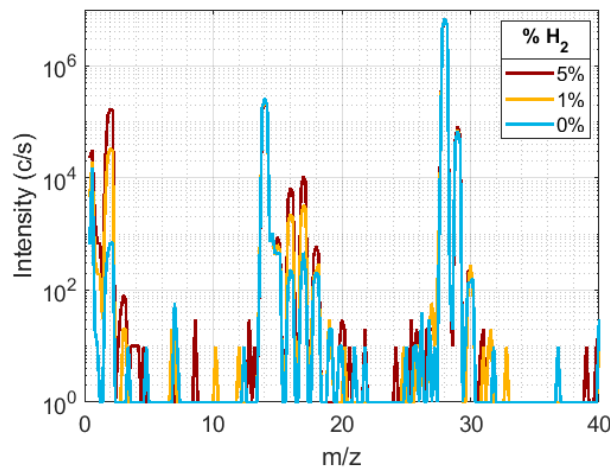


**Figure 4.** MS spectra during plasma (0.91 mbar,  $\sim 11$  W) in  $\text{N}_2$  and  $\text{N}_2$ - $\text{H}_2$  at different percentages of  $\text{H}_2$ .  $\text{N}_2$  has fragments at  $m/z$  7, 14, 15, 28, 29, 30.  $\text{H}_2$  is visible at  $m/z$  2.  $m/z$  16 and 17 are mainly associated to ammonia. Traces of water are detected at  $m/z$  18. The lower detection limit is at  $\sim 30$  c/s.

MS are highly sensitive to their electrical environment and measured intensities can drift. To avoid any changes in the global intensity due to charging effects by the plasma, intensities were divided by a reference peak in the spectra. We chose  $m/z$  14, a dissociation peak of  $\text{N}_2$  which is closer to the  $m/z$  17 peak of  $\text{NH}_3$  than  $m/z$  28.

At the ignition of the discharge, close to the confining box, the ammonia amount roughly stabilizes in 2-3 minutes. However, ammonia tends to adsorb on the metallic walls of the chamber and the homogenization of ammonia in the chamber takes several tens of minutes depending on the surface state of the walls and the plasma parameters. Simultaneous measurements of ammonia by IR spectroscopy and MS spectrometry are therefore both started 30 min after the ignition of plasma, and integrated over 1.5 to 3 hours (depending on the parameters for the IR spectrum acquisition).

We performed two calibrations at two different pressures (see appendix A2). The precision is limited by the IR measurement ( $\pm 10\%$ ). The evolution of the calibration coefficient between  $\text{NH}_3$  density and  $m/z$  ratio 17/14 is linear with pressure.

#### 2.4.3 Measurements of ammonia density by mass spectrometry

Once the MS is calibrated at  $m/z$  17 thanks to IR spectroscopy, it is useful to measure fast and local modifications of ammonia density in the chamber. The influence of  $\text{H}_2$  percentage, RF plasma voltage and pressure are studied.

As ammonia tends to adsorb on the reactor walls, a great care was taken to have a clean wall surface state before each experiment. After a long exposure to plasma, walls are heated for several hours to eliminate residual ammonia. However, we observed that for short plasma durations (11 min), the use of a high vacuum pump between two experiments is sufficient. The MS took continuous measurements on a few selected masses (at  $m/z$  14, 16, 17, 18, 28), starting 30 s before the ignition of the plasma and continuing during the 10 following minutes of the discharge. Ammonia intensity is roughly stable after a few minutes (see appendix A3). The intensity was integrated over the last few minutes where the signal is stable to get the final value for the deduction of the  $\text{NH}_3$  density.

## 2.5 Positive ions measured by mass spectrometry

The positive ion mode of the MS is used to detect positive ions formed in the discharge. A small hole is pierced in the confining box and the collecting head of the MS is positioned in front, in contact with the box to keep the plasma confined inside. Consequently, the MS measures ions present next to the walls inside the confining box, at  $\sim 1$  cm from the upper polarized electrode. The collecting hole of the mass spectrometer and the confining box are both at the ground. Figure 5 shows typical MS spectra taken in ion mode in  $\text{N}_2$  and  $\text{N}_2\text{-H}_2$  plasmas.

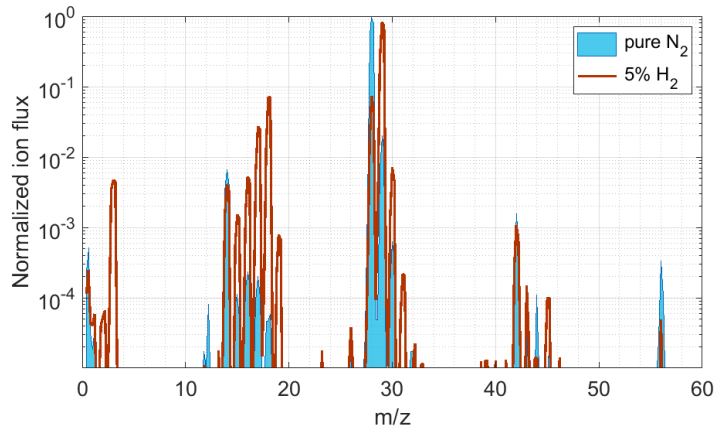


**Figure 5.** MS normalized spectra of ions in  $\text{N}_2$  and  $\text{N}_2 - 5\% \text{H}_2$  discharges, at 0.86 mbar (55 sccm) and for an absorbed power of  $\sim 11$  W (406  $V_{\text{RF,pp}}$ )

$m/z$	corresponding ion	$m/z$	corresponding ion
2	$\text{H}_2^+$	28	$\text{N}_2^+$
3	$\text{H}_3^+$	29	$\text{N}_2\text{H}^+$ / isotope $\text{N}_2^+$
14	$\text{N}^+$	30	$\text{N}_2\text{H}_2^+$ / isotope $\text{N}_2\text{H}^+$
15	$\text{NH}^+$ / isotope $\text{N}^+$	42	$\text{N}_3^+$
16	$\text{NH}_2^+$	43	$\text{N}_3\text{H}^+$
17	$\text{NH}_3^+$	44	$\text{N}_3\text{H}_2^+$
18	$\text{NH}_4^+$	45	$\text{N}_3\text{H}_3^+$
19	isotope $\text{NH}_4^+$ / $\text{H}_3\text{O}^+$	56	$\text{N}_4^+$

**Table 1.** Selected ions for the study

MS acquisition parameters tuned for each mass are the same for  $m/z$  from 14 to 56, but are different for  $m/z$  2 and 3. Therefore, for optimized measurements for all  $m/z$ , we used two different sets of parameters: one

optimized for  $m/z$  2 and 3, and one optimized for the others  $m/z$ . At such low power conditions, only ions with a charge  $z=1$  are expected to be detected. Selected ion peaks at given  $m/z$  values (see figure 5 and table 1) are measured in continuous acquisition by the MS in ion mode from the ignition of the plasma and until stabilization of the signal. The intensity of each ion is then averaged over few minutes after stabilization of the signal (from ~8 to 10 min, see appendix A3).

MS does not give reliable absolute values for ion. Indeed, the intensities measured depend strongly on MS selected parameters and sometimes vary during the acquisition due to charging effects. Therefore, we provide only relative intensity values. In the following, ion intensities (or fluxes) are normalized by the total intensity (or flux) measured for ions, which is approximated by the sum of the intensities measured for  $m/z$  28, 29, 17, 18 and 14 (see figure 5).

The  $^{15}\text{N}$  isotope of nitrogen is usually 0.36% of nitrogen atoms, and can therefore be detected by the MS, especially in pure  $\text{N}_2$  at  $m/z$  15 ( $^{15}\text{N}^+$ ), 29 ( $^{14}\text{N}^{15}\text{N}^+$ ) and 30 ( $^{15}\text{N}^{15}\text{N}^+$ ) (see table 1). In  $\text{N}_2\text{-H}_2$  discharges, it can also influence intensity measurements at  $m/z$  19 ( $^{15}\text{NH}_4^+$ ) and 30 ( $^{14}\text{N}^{15}\text{NH}^+$ ). Isotopes are therefore taken into account to study the intensities of other ions at  $m/z$  15, 19, 29 and 30. Water has a strong proton affinity and  $\text{H}_2\text{O}$  adsorbed in small quantities on the walls in the reactor easily forms  $\text{H}_3\text{O}^+$ , which contributes at  $m/z$  19. As  $\text{H}_2\text{O}^+$  ( $m/z$  18) should be present in far lower quantities than  $\text{H}_3\text{O}^+$ , the strong signal at  $m/z$  18 can be entirely attributed to  $\text{NH}_4^+$ . Impurities from air should be seen at  $m/z$  32 ( $\text{O}_2^+$ ) and  $m/z$  44 ( $\text{CO}_2^+$ ) in both pure  $\text{N}_2$  and  $\text{N}_2\text{-H}_2$  plasmas. Figure 5 confirms that they can be neglected in this study.

## 2.6 Mass dependence of the mass spectrometer transmission

In both neutral and ion modes, intensities measured by the MS at different  $m/z$  cannot be directly compared as the ionization, the flight in the MS through the quadrupole and the detection depend on the mass and the intrinsic properties of the species. A transmission curve has been obtained for the MS used in this work. Many transmission curves of MS can be found in the literature: for EQP MS from Hiden equipped with SEM [46–48] or for other MS [35,49,50]. They use the method described below, always using several gases among  $\text{H}_2$ , He, Ne,  $\text{N}_2$ ,  $\text{O}_2$ , Ar, Kr and Xe. As a transmission curve depends strongly on the MS configuration, the curves obtained in the literature vary from one another. Transmission is mainly decreasing with  $m/z$ , as we found for the MS used here in the case of a tune on  $m/z$  2 (see appendix A4).

### 2.6.1 Calibration for neutrals

Different gases (or gas mixtures in well-known proportions) were injected in the chamber. The transmission of the MS at the mass of the studied gas is deduced from the comparison of the intensity measured by the MS and its partial pressure in the chamber. As the temperature ( $T$ ) is the same for all neutrals, the density of an atom or molecule is directly linked to its partial pressure. The transmission curve as a function of mass is obtained once the measurement is done with different gases at various masses. For better accuracy, several measurements were performed for a same gas at different pressures. Then, the slope of the intensity as function of the partial pressure was used for the transmission curve.

The intensity measured by the MS ( $I_{\text{MS}}$ , in count/s) at the  $m/z$  of an atom/molecule  $X$  is linked to its partial pressure in the chamber ( $P_{X,0}$ ) by the following equation:

$$I_{\text{MS}}(m_X) = \frac{P_{X,0}}{k_B \cdot T} \times T_{\text{ap}}(m_X) \times T_{\text{ioni},X} \times T_{\text{MS}}(m_X) \times \frac{1}{K_{\text{iso},X}} \quad (3)$$

with  $T_{\text{ap}}$  the transmission through the 100  $\mu\text{m}$  aperture of the MS,  $T_{\text{ioni},X}$  the transmission through the ionization chamber,  $T_{\text{MS}}$  the transmission through the MS (lenses, quadrupole, detector) at the main mass of  $X$ , and  $k_B$  the Boltzmann constant. A coefficient  $K_{\text{iso},X}$  is introduced to take all the isotopes of the atom/molecule  $X$  into

account, from the measurement of the main peak only. Isotopes abundances are measured and are congruent with values found on the NIST database.

The flow through the 100  $\mu\text{m}$  aperture of the MS is in between the free molecular regime and the viscous regime, with a Knudsen number  $\sim 1$ . Therefore, the transmission of the atom/molecule X through the pin hole depends on both its mass ( $m_x$ ) and the average mass of the carrier gas ( $m_{\text{avg}}$ ) [51–53]. Details are given in appendix A4.

$$T_{ap}(m_X) \equiv \frac{n_{X,MS}}{n_{X,0}} = \frac{P_{X,MS}}{P_{X,0}} \propto \frac{C_{\text{visc}}}{\sqrt{m_{\text{avg}}}} + \frac{0.38}{\sqrt{m_X}} \quad (4)$$

with  $C_{\text{visc}} = 0.46$  for atoms and  $C_{\text{visc}} = 0.49$  for diatomic molecules and methane.

The ionization source used is based on electronic impact with electrons accelerated at 70 eV. The ionization of species by such an ionization source also leads to the formation of double charged species, and fragments (if there are several atom). Some fragments or double ionized species can be an important percentage of the total ionized species formed. However, it depends strongly on the ionization source used, its tuning and its ageing. Therefore, we avoid to take them into account, and we consider only the simple ionization process on the atom/molecule X:  $X + e^- \rightarrow X^+ + e^- + e^-$ . Consequently, we use the simple ionization cross section at 70 eV ( $\sigma_x$ ) to link the partial pressure of the atom/molecule X in the MS ( $P_{x,MS}$ ) to the ion flux formed by ionization ( $j_{x^+,MS}$ , in  $\text{s}^{-1}.\text{m}^{-2}$ ) (see details in appendix A4):

$$T_{\text{ioni}}(X) \equiv \frac{j_{X^+,MS}}{P_{X,MS}} = \sigma_X \times cst \quad [\text{m}^{-2}.\text{s}^{-1}.\text{Pa}^{-1}] \quad (5)$$

Ionization cross sections are hard to measure and model: their values have large uncertainties which affect the calibration. It is especially the case for molecular gases that can fragment. Values given for simple ionization coefficients by different sources are compared in table 2: results of computations with the databases of Biagi (program Magboltz) [54] and IST-Lisbon [55,56], and measurements with Phelps database [57–62]. For consistency, we always used Phelps database values when they exist.

Gas	Simple ionization cross section $\sigma$ ( $\text{\AA}^2$ )	Estimated uncertainty on $\sigma$ (+/- %)	Isotope corrective coefficient $K_{\text{iso}}$
H <sub>2</sub>	0.935 (Biagi) 0.967 (IST) <b>0.967</b> (Phelps)	10	1.000
N <sub>2</sub>	2.33 (Biagi) 1.92 + 0.23 (IST) <b>2.15 + 0.17</b> (Phelps)	20	1.007
CH <sub>4</sub>	<b>1.95</b> (IST)	30	1.016
O <sub>2</sub>	2.38 (Biagi) 2.8 (IST) <b>2.36</b> (Phelps)	20	1.005
He	0.313 (Biagi) 0.322 (IST) <b>0.313</b> (Phelps)	10	1.000
Ne	0.490 (Biagi) <b>0.514</b> (Phelps)	10	1.105
Ar	2.77 (Biagi) 2.77 (IST) <b>2.7</b> (Phelps)	10	1.0035
Kr	<b>4.21</b> (Biagi)	10	1.767
Xe	<b>5.3</b> (Biagi)	10	3.706

**Table 2.** Simple ionization cross sections of gases used for calibration.

We computed the total transmission at the mass  $m_x$  through the aperture, the ionization chamber and the MS lenses, quadrupole and detector, as done in [49]:

$$T_{tot}(m_x) = \frac{I_{MS}(m_x) \times K_{iso,X}}{\sigma_X \times P_X} \quad [ct.s^{-1}.m^{-2}.Pa^{-1}] \quad (6)$$

with  $P_x$  the partial pressure of the atom/molecule X. The final calibration curve is given in figure 6.a. It is well-fitted by a log-normal law:

$$f(x; G, \mu, s) = \frac{G}{x \cdot s \cdot \sqrt{2\pi}} \cdot \exp\left(-\frac{(\ln(x) - \mu)^2}{2s^2}\right) \quad (7)$$

with  $G = 290\,000$ ,  $\mu = 3.42$  and  $s = 1$ .

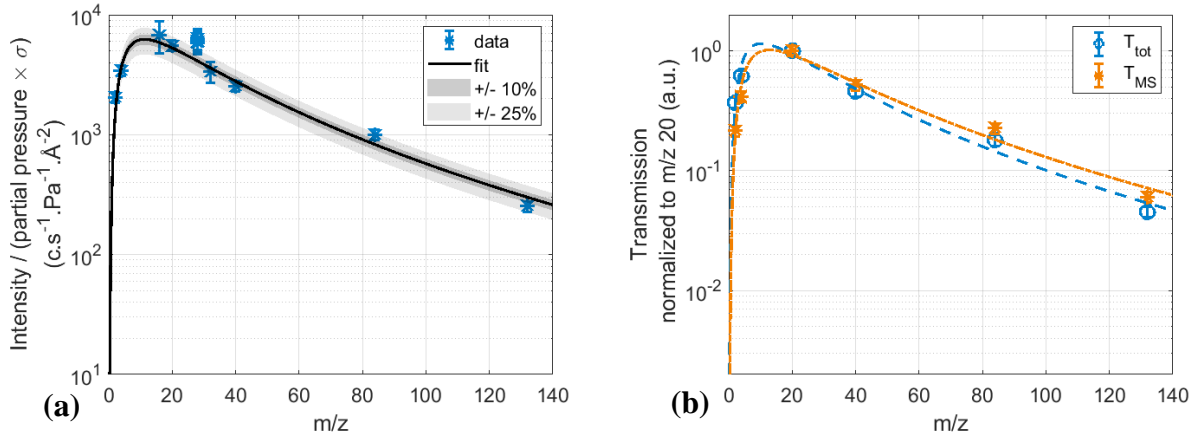


**Figure 6.** Transmissions through the MS, obtained for a set of parameters tuned on  $m/z$  28. Data points correspond to the following gases at their respective  $m/z$ : H<sub>2</sub> (2), He (4), CH<sub>4</sub> (16), Ne (20), N<sub>2</sub> (28), O<sub>2</sub> (32), Ar (40), Kr (84) and Xe (132). (a) Total transmission and its error bars. (b) Comparison of the normalized transmissions  $T_{tot}$  and  $T_{MS}$ , fitted by log-normal laws with the following parameters:  $G_{tot} = 52$ ,  $G_{MS} = 55$ ,  $\mu_{tot} = 3.4$ ,  $\mu_{MS} = 3.6$  and  $s_{tot} = s_{MS} = 1$ .

The transmission curve  $T_{tot}(m)$  can be directly used to retrieve a neutral partial pressure (and density) from a MS measurement and equation (6), knowing its simple ionization cross section and  $K_{iso,X}$ . This transmission curve has been obtained for a given set of parameters of the MS, corresponding to a tune that optimizes  $m/z$  28. It changes when parameters are changed. In particular, it is very different for parameters tuned on  $m/z$  2 (see appendix A4). In both cases, calibration curves have a steep slope at low  $m/z$ . To avoid any possible large errors, we do not compare intensities at  $m/z$  2 and 3 with the higher  $m/z$ .

It is also possible to get information on the ion flux generated inside the MS, thanks to  $T_{MS}$ . Indeed:

$$T_{MS}(m_x) \equiv \frac{I_{MS}(m_x)}{j_{X^+,MS}} \quad [ct.m^2] \quad (8)$$

$T_{MS}(m)$  can be obtained from  $T_{tot}(m)$  (figure 6.a) and a model of  $T_{ap}(m)$  (equation (4)). For simplicity, we will work with relative ion fluxes. Consequently, only the dependence in mass of the transmission has to be considered. The expression of  $T_{MS}(m)$  is obtained using equations (3), (4) and (6). It is plotted in figure 6.b.

$$T_{MS}(m_x) = \frac{k_B T}{cst1} \times \frac{T_{tot}(m_x)}{T_{ap}(m_x)} \propto \frac{T_{tot}(m_x)}{\frac{C_{visc}}{\sqrt{m_{avg}}} + \frac{0.38}{\sqrt{m_x}}} \quad (9)$$

### 2.6.2 Calibration for positive ions

In the case of ions, there is no ionization source, but the addition of a high voltage just after the entrance of the MS (named the ‘extractor’) and an associated lens (named ‘lens 1’) to focus the incoming ions into the MS. It is far more complex to directly obtain a transmission curve for ions as it is not usually easy to quantify ion densities or fluxes. Therefore, transmission curves for ions are usually deduced from transmission curves obtained with neutrals [35,48,53].

The transmission of ions through the lenses (except lens 1), the quadrupole and the detector is the same as in RGA mode:  $T_{MS}$  is the same as the one calibrated above. As we work with ion fluxes, no change is expected from the passage through the 100  $\mu\text{m}$  aperture [63]. The only part to study is the travel of ions through the extractor and lens 1: do they induce a mass-dependent transmission of ions? To address this issue, we studied the passage of ions of different masses through the extractor and lens 1.

When the value of the extractor is changed, lens 1 should be adapted, but also the parameter ‘energy’, which is linked to the energy distribution of the ions measured. In a  $\text{N}_2\text{-H}_2$  plasma, for a given absolute value of the extractor below  $\sim 60$  V, all ions have a similar energy distribution (see appendix A4). There is only an exception for low  $m/z$  (e.g.  $\text{H}_3^+$ ). Therefore, we do not recommend to compare measurements done at low  $m/z$  with the others.

For absolute values of the extractor below  $\sim 60$  V, the relation between the extractor and lens 1 is linear, and the scans of lens 1 for different  $m/z$  superimpose, except for lower  $m/z$  (see figure 7). In conclusion, for absolute values of the extractor below 60 V, one should reasonably say that lens 1 focuses similarly all the ions ( $< 20\text{-}30\%$  error) except the ions with low masses (below  $m/z \sim 5\text{-}10$ ).

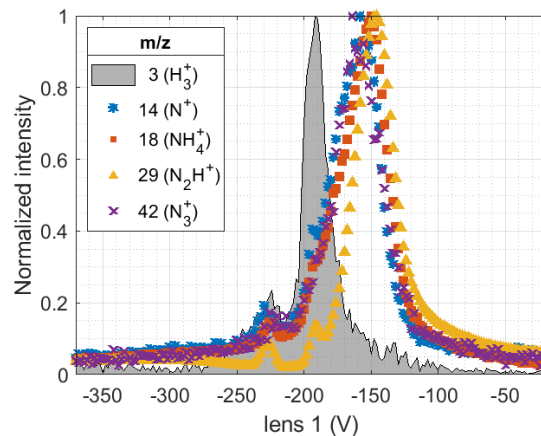


**Figure 7.** Scans of the MS parameter lens 1 for different ions, in a  $\text{N}_2\text{-H}_2$  plasma at 0.80 mbar, the extractor being fixed to  $-40$  V.

Ions in the MS undergo a supplementary process in ion mode than in RGA mode: the passage through the extractor and lens 1. At high potential of the extractor, ion energy is likely to change. As lens 1 focuses similarly all the ions (except very low masses) for absolute values of the extractor below 40-60 V, we can expect that the group formed by the extractor and lens 1 has a transmission independent on mass in these conditions (at least  $< 20\text{-}30\%$  modifications).

Therefore, to compare ions measured on a same mass spectrum, with similar energies, we can use the above transmission curve  $T_{MS}$ , obtained in RGA mode. It is valid for ions with  $m/z$  larger than  $\sim 10$ , and with a potential lower than  $\sim 60$  V on the extractor. For an ion  $\text{X}^+$  present in the chamber, leading to an intensity of  $I_{MS}(m_x)$  [ct/s] detected by the MS, the relative ion flux in the chamber can be deduced by:

$$\frac{j_{X^+,0}}{j_{tot^+,0}} = \frac{j_{X^+,MS}}{j_{tot^+,MS}} = \frac{I_{MS}(m_X)}{T_{MS}(m_X)} \times \frac{1}{\sum_i \frac{I_{MS}(m_i)}{T_{MS}(m_i)}} \quad (10)$$

The ion flux then computed is the ion flux, at the entrance of the MS. A sheath forms on the MS collector head, and accelerates the ions towards the surface. Therefore, the ion flux measured is not equal to the ion flux in the bulk of the plasma discharge. [49] developed a simple model to take the sheath effect into account, to deduce the ion flux in the bulk, as well as the ion densities from the electron density. In the case of PAMPRE, the 2D ion distribution is studied by a more complex model, detailed in paper II.

### 3. Results

Essentially three experimental parameters are varied to test their effect on the measurements. The H<sub>2</sub> percentage in the N<sub>2</sub>-H<sub>2</sub> gas mixture varies from 0 to 5%. Pressure is varied from 0.33 to 0.91 mbar by changing the gas flow (from 10 to 70 sccm). RF peak-to-peak voltage is varied between 254 and 483 V.

#### 3.1 Electrical measurements and electron density

In the following figures, error bars take into account the accuracy and the measurements repeatability. Measurements are done at several selected peak-to-peak RF voltages ( $V_{RF,pp}$ : 254, 326, 367, 406 and 483 V). However, as mentioned in [38] the most relevant plasma parameter for the comparison between experiment and model is the RF power absorbed by the plasma ( $W_{eff}$ ). The RF power measurements with the digital V-I probe (Solayl) ( $\pm 0.5$  W) are much more accurate than measurements done in [38] ( $\pm 2$ W). The measured absorbed power is given for all the conditions studied and plotted according to the RF peak-to-peak voltage in figure 8 (a).

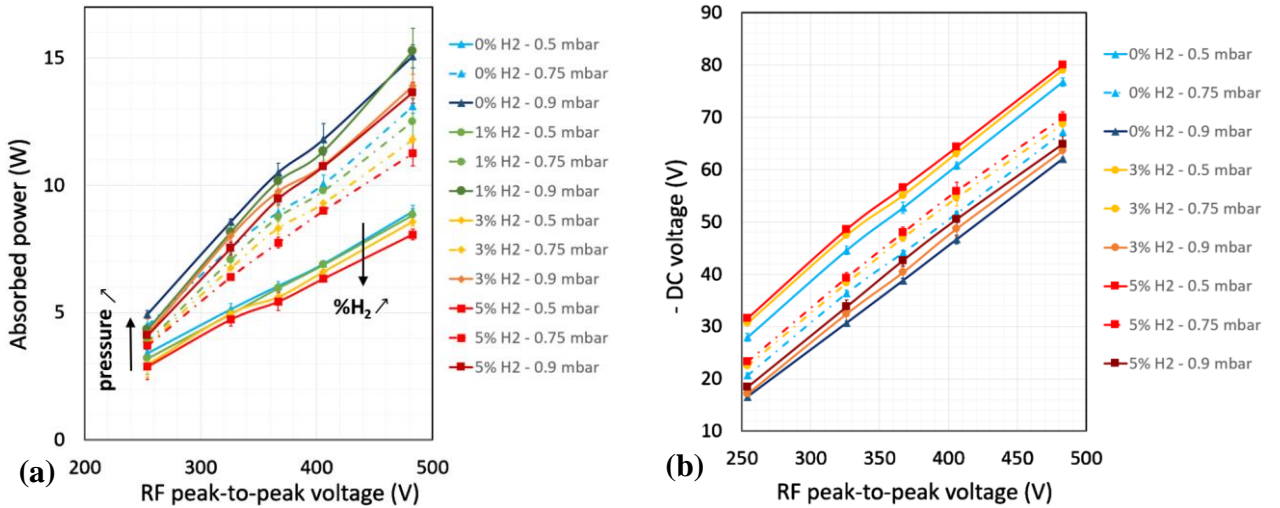


**Figure 8.** (a) RF power absorbed by the plasma and (b) self-bias potential  $V_{DC}$  as function of  $V_{RF,pp}$  in all the conditions studied here (various  $V_{RF,pp}$ , % of H<sub>2</sub> and pressure).

Absorbed power increases systematically with the RF peak-to-peak voltage. However, H<sub>2</sub> amount and pressure also have an effect on its value. At a given percentage of H<sub>2</sub> and a given  $V_{RF,pp}$ , the absorbed power increases strongly with pressure. At a given  $V_{RF,pp}$  and pressure, the absorbed power decreases slightly with the amount of H<sub>2</sub>.

The figure 8 (b) presents the self-bias potential ( $V_{DC} < 0$  in this configuration) for all the experimental conditions. These measurements are fundamental to validate the model described in paper II. The experiments show a linear dependence of  $|V_{DC}|$  against  $V_{RF,pp}$ , with a constant slope of 0.2 in all conditions of pressure and hydrogen content. The variation of  $|V_{DC}|$  with the discharge parameters relates to changes in the ion current [64]. In an asymmetric reactor, a higher ion current increases the asymmetry in the collection of charges at the electrodes, leading to a higher  $|V_{DC}|$ . At high  $V_{RF,pp}$  the absorbed power increases, inducing an increase in the electron density (cf figure 9.a), the ion current and thus  $|V_{DC}|$ . On the other hand, an increase in the pressure leads to the reduction of the sheath thickness [64], implying a decrease in the ion current and  $|V_{DC}|$ , consistent with previous observations in pure N<sub>2</sub> [38].

The figure 9 (a) presents electron density results as a function of absorbed RF power. The experiments show that the electron density increases exponentially with  $W_{eff}$ . At a given  $W_{eff}$ , an increase in the pressure leads to lower electron densities, but the exponential behavior is maintained. For pure N<sub>2</sub> the  $n_e$  values are globally in agreement with published values in [38]. According to the model detailed in paper II, the exponential increase is due to plasma interaction with surfaces, leading to the production of secondary electrons.

The percentage of H<sub>2</sub> in the mixture does not have any effect on the electron density, except for the higher  $W_{eff}$  cases. For high  $W_{eff}$ , despite large error bars, it seems that the increase of hydrogen content leads to an increase of the electron density at a given pressure. This point is discussed in paper II. The ionization degree is obtained from the electron density by dividing by the total neutral density. Figure 9 (b) shows that trends are the same as for electron density.

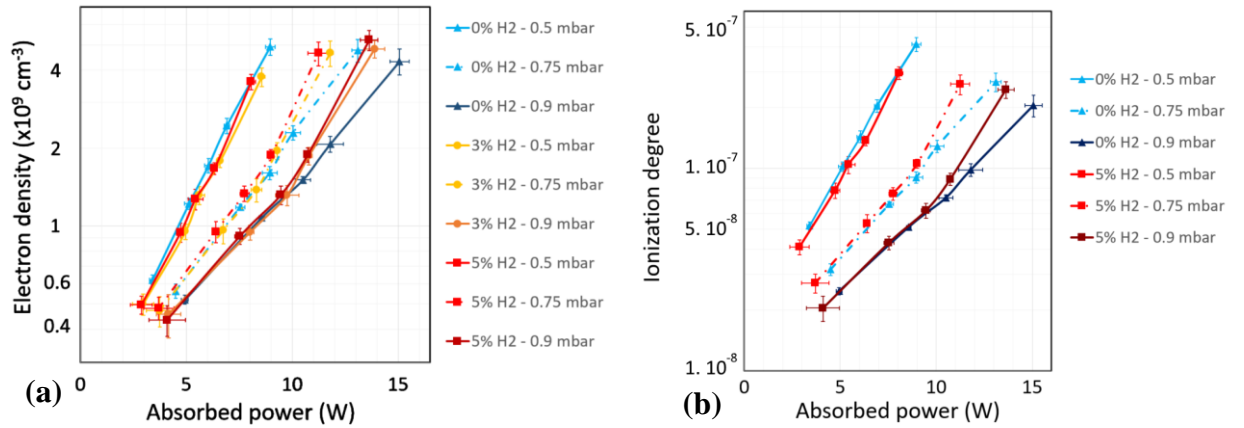


**Figure 9.** (a) Electron density and (b) ionization degree measured for several experimental conditions.

### 3.2 Ammonia density

Ammonia is the most stable molecule formed in a N<sub>2</sub>-H<sub>2</sub> plasma. The abundance of ammonia is a major constraint in the chemistry of the plasma (see paper II). A study of the formation of NH<sub>3</sub> depending on the different discharge conditions is shown in figure 10. For each condition NH<sub>3</sub> density is given in absolute values. An uncertainty of 20% is indicated on the graphs, evaluated from the uncertainty on the calibration coefficient and the MS measurements.

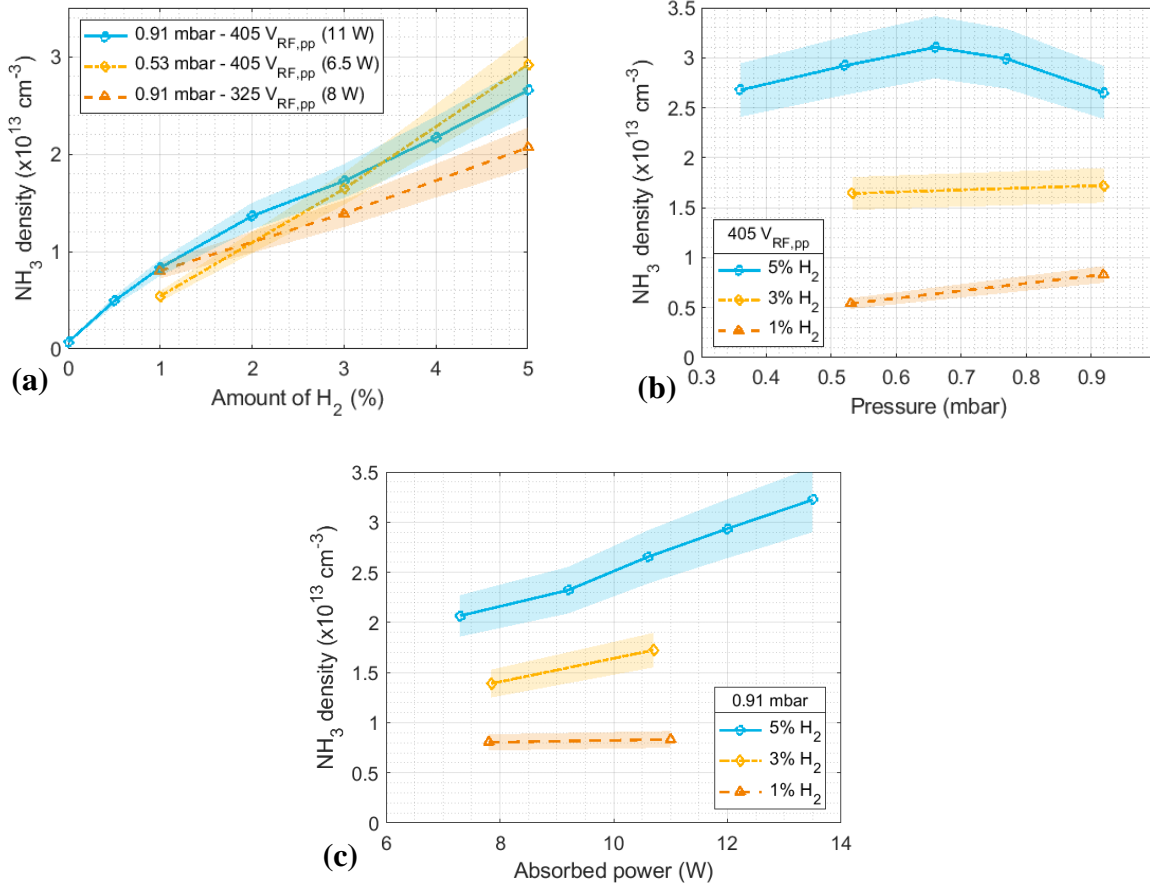


**Figure 10.** NH<sub>3</sub> amount as function of injected H<sub>2</sub> (a), pressure (b) and absorbed power (c).

Ammonia density increases linearly with the percentage of H<sub>2</sub> in N<sub>2</sub>. It also increases slightly with the absorbed power. However, the absolute density of NH<sub>3</sub> is constant with pressure from 0.35 to 0.9 mbar. This suggests that ammonia density is controlled by surface processes, as discussed in [30,31] and in paper II.

### 3.3 Positive ions

The positive ions give important indications on the gas phase chemistry happening in the plasma and on nearby surfaces. They have been measured two to four times for each of the selected experimental conditions. Following figures present the average data points for each condition. Error bars are estimated from the reproducibility of the measurements and an uncertainty on the MS calibration estimated to  $\pm 20\%$  (see section 2.6). These error bars take into account the instrumental (charging effects) and plasma effects (stabilization of the ion fluxes in the plasma as presented in appendix A3, variations of the impurities quantity...). The following figures present the evolution of ion fluxes with the parameters of the experiment (H<sub>2</sub> amount, pressure and absorbed power). These are the ion fluxes at the entrance of the MS. The 2D ion densities inside the reactor chamber are retrieved by the model presented in paper II.

Figure 11 shows the evolution of relative ion fluxes with the percentage of  $H_2$  in the plasma. As explained in part 2.6, the analysis of  $m/z$  2 and 3 is separated from the others. No calibration is applied to correct these measurements at low  $m/z$ , therefore no quantitative comparison can be done with the other  $m/z$ . For reproducibility (see part 2.5), the ion measurements are normalized to the sum of all ion fluxes (or to the sum of all intensities in the case of  $m/z$  2 and 3).

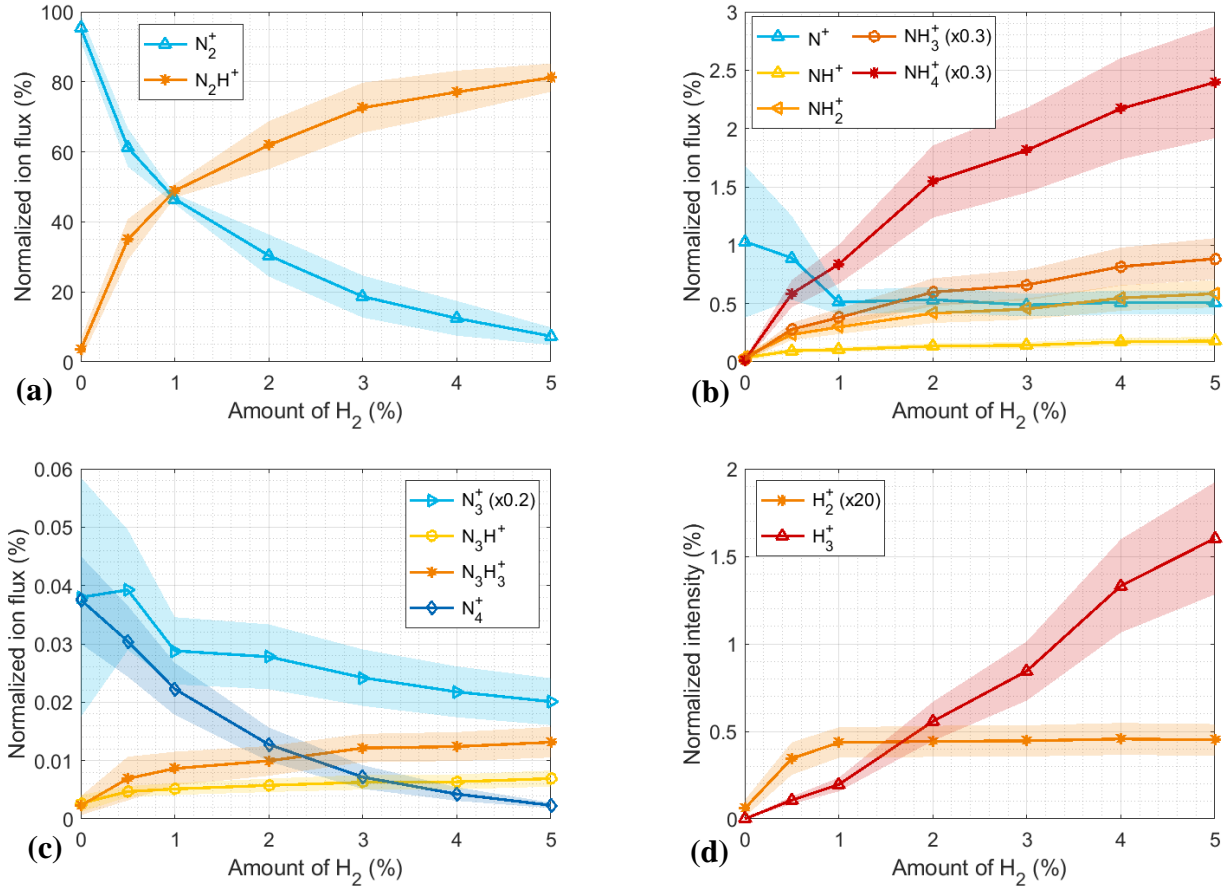


**Figure 11.** Normalized positive ion fluxes (a,b,c) or intensities (d) as function of the percentage of  $H_2$  injected in the experiment. Conditions with 0.9 mbar (55 sccm) and  $\sim 10$  W absorbed power (405 V<sub>RF,pp</sub>).

The amount of  $H_2$  injected in the plasma has a strong impact on the ions produced. In pure  $N_2$  plasma,  $N^+$ ,  $N_2^+$ ,  $N_3^+$  and  $N_4^+$  are detected. These ions formed with only nitrogen decrease as soon as a small quantity of  $H_2$  is injected in the plasma.  $N_2^+$  and  $N_4^+$  have nearly disappeared with 4-5% of  $H_2$ .  $N^+$  and  $N_3^+$  on one side, and  $N_2^+$  and  $N_4^+$  on the other side, have similar trends. Their formation and/or stabilization processes are linked.

On the other hand, new species containing hydrogen appear: nitrogen ions become protonated thanks to the injection of hydrogen. The  $H_3^+$  ion increases linearly with the injected  $H_2\%$ , no saturation effect is seen for values of hydrogen inferior to 5%. On the contrary,  $H_2^+$  stabilizes as soon as 1% of  $H_2$  is injected in the experiment.  $N_xH_y^+$  ions form in the presence of hydrogen, but their growth is not linear with the amount of  $H_2$ : their formation is limited by another variable than the quantity of hydrogen, contrarily to  $H_3^+$ . Especially,  $N_2H^+$  tends toward saturation at  $\sim 5\%$  of  $H_2$ . Its evolution is anti-correlated with the one of  $N_2^+$ : its formation is limited by the available quantity of ionized nitrogen. At 5%  $H_2$  (at 0.9 mbar and  $\sim 10$  W),  $N_2^+$  decreases at 7.3% and the major ions after  $N_2H^+$  (78%) are the ions  $NH_4^+$  (10%) and  $NH_3^+$  (3.7%) leading to the formation (or formed thanks to) ammonia. This is consistent with observations by [35] in a ICP discharge, where  $N_2H^+$  is predicted to be dominant for percentages of  $H_2$  lower than 60%,  $NH_4^+$  and  $NH_3^+$  being dominant for  $H_2$  amounts above this value.

Ion populations are modified by the variation of pressure (induced by the variation of the gas flow from 10 to 70 sccm). Results are presented on figure 12.

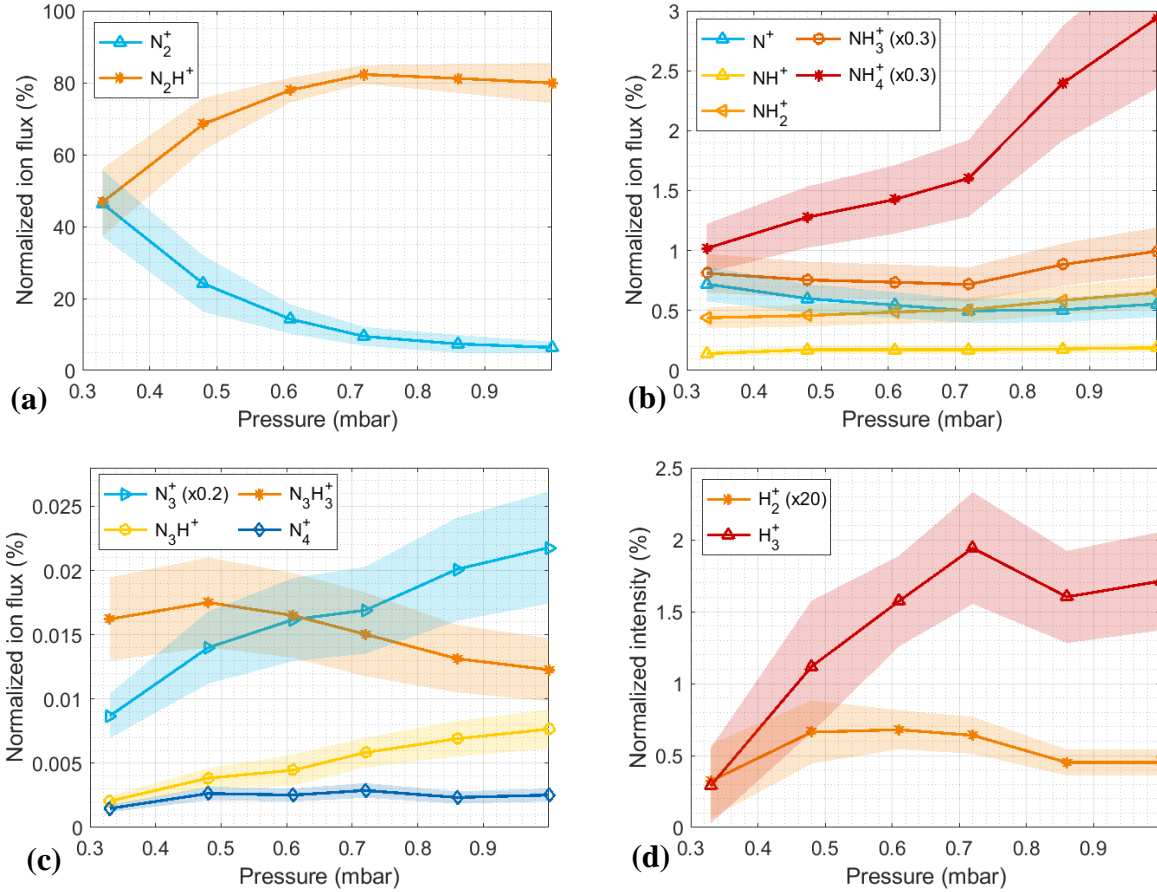


**Figure 12.** Normalized positive ion fluxes (a,b,c) or intensities (d) as function of pressure. Conditions with 5%  $H_2$  and 6-11 W absorbed power (405  $V_{RF,pp}$ ).

The increase of the gas flow (and therefore the pressure) leads to an increase of nearly all the ions, except  $N_2^+$  and  $N^+$ . Especially, at 0.33 mbar,  $N_2^+$  and  $N_2H^+$  have equal fluxes. It seems that at higher pressures, more complex and/or protonated ions are formed and/or transported in higher quantities to the walls of the confining box where the measurement is done.  $N_2H^+$ ,  $NH_4^+$ ,  $H_3^+$ , and in smaller proportions  $N_3^+$ ,  $N_4^+$  and  $N_3H^+$  increase clearly with pressure, while  $H_2^+$ ,  $NH^+$ ,  $NH_2^+$  and  $NH_3^+$  stay rather constant. This can be easily explained by the fact that  $N_2H^+$ ,  $NH_4^+$ ,  $H_3^+$ ,  $N_3^+$ ,  $N_4^+$  and  $N_3H^+$  require a reaction between an ion (or radical) and a neutral gas phase molecule to form, whereas  $H_2^+$ ,  $N_2^+$ ,  $N^+$ ,  $NH^+$ ,  $NH_2^+$  and  $NH_3^+$  can be simply formed by direct ionization of neutrals  $H_2$ ,  $N_2$  and  $NH_3$  (see table of reactions in paper II). With the increase of pressure, ion – neutral collisions increase and consequently ions formed from such collisions are formed in higher proportions compared to ions formed by direct ionization (see figure 14). Similar observations are discussed in [31].

Ions are also influenced by the power absorbed by the plasma (see figure 13).

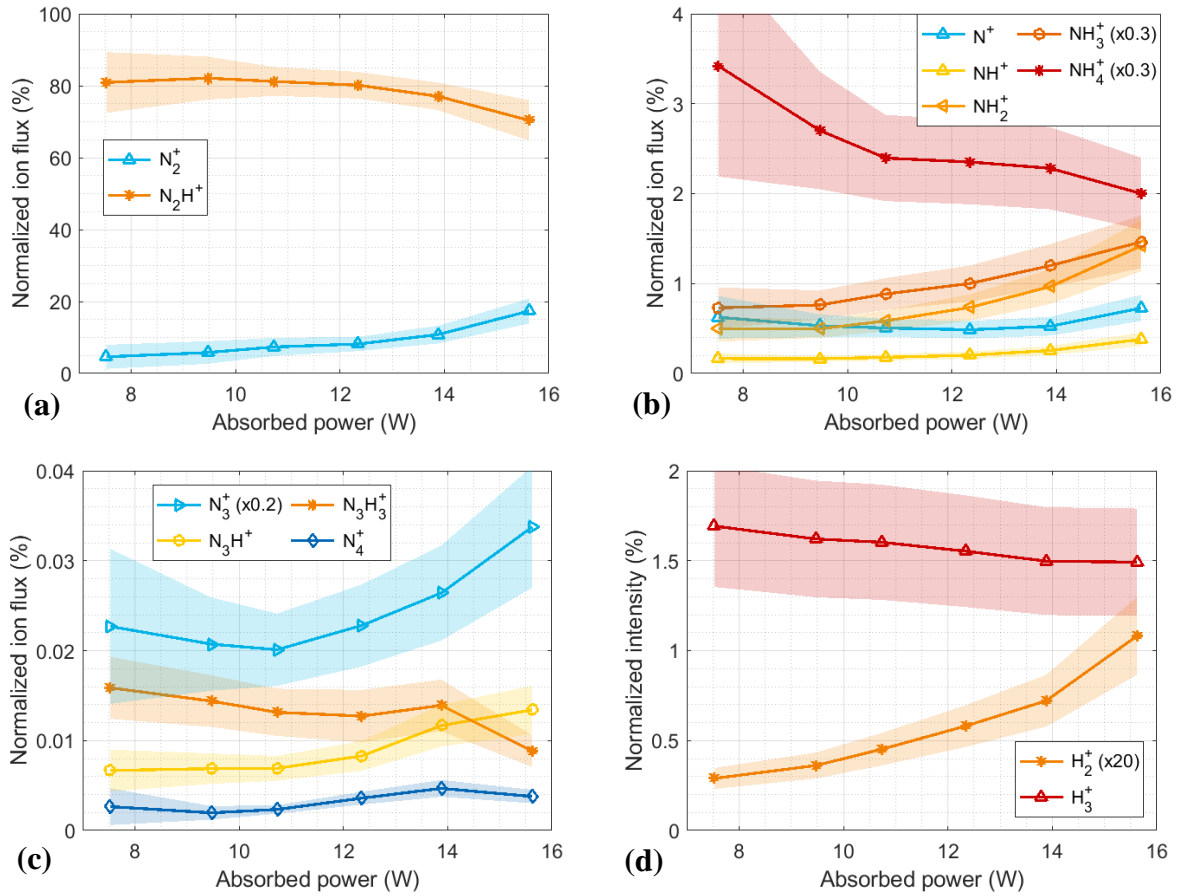


**Figure 13.** Normalized positive ion fluxes (a,b,c) or intensities (d) as function of the power absorbed by the plasma. Conditions with 5%  $H_2$  and 0.9 mbar (55 sccm).

The increase of absorbed power moderately impacts the positive ion relative fluxes. However, the electron density increases, consequently the total ion density should increase similarly. A decrease of the relative intensities is observed for some species formed by ion (or radical) – neutral processes: of 10% for  $H_3^+$ ,  $N_2H^+$ ,  $N_3H_3^+$  and 40% for  $NH_4^+$ . On the contrary, species formed by direct ionization increase:  $H_2^+$ ,  $NH^+$ ,  $NH_2^+$ ,  $NH_3^+$ ,  $N_2^+$ . Contrarily to the increase of pressure, an increase of power favors the formation of species by direct ionization (see figure 14). A small relative increase of  $N_3^+$ ,  $N_3H^+$  and  $N_4^+$  can also be noted.

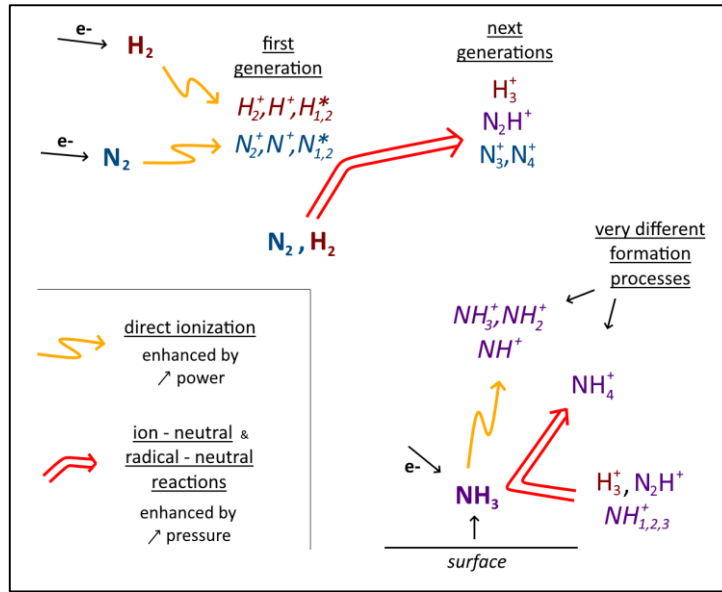


**Figure 14.** How coupled power and pressure affect ion formation: the main reactions.

## 4. Conclusion

In this work, a RF CCP discharge in nitrogen with small amounts of hydrogen (up to 5%), at low coupled power (3 to 13 W) and low pressure (0.3 to 1 mbar) is experimentally characterized. Electrical parameters, electron density, ammonia density and positive ions are measured in various different plasma conditions. One of the objectives is to form a complete dataset for the implementation of hydrogen-linked processes in the model of pure  $\text{N}_2$  RF CPP discharge described in [38]. The model is described in paper II and the reader should refer to it for more details.

A complete study of the MS transmission curve has been performed to deduce relative ion fluxes from MS measurements. The main conclusion is that transmission curves depend on the set of MS parameters. In particular, sets of parameters obtained for a tuning on small  $m/z$  (as 2) lead to MS transmissions very different than if tuned on larger  $m/z$  (as 28).

The addition of hydrogen in an initially pure  $\text{N}_2$  discharge induces some electrical changes. A 10-15% decrease of the coupled power for a same peak-to-peak RF potential is observed. However, the electron density stays rather constant with the  $\text{H}_2$  amount, except for the higher pressure and power cases, where it could increase up to 25% with the addition of 5% hydrogen.

Concerning the molecular plasma species, the addition of  $\text{H}_2$  has the expected effect to hydrogenate nitrogen ions, and lead to the formation of  $\text{NH}_3$ .  $\text{N}_2\text{H}^+$  is the major ion in the discharge for  $\text{H}_2$  amounts above 1% (~78% for 5% injected  $\text{H}_2$ ), while  $\text{NH}_3^+$  and  $\text{NH}_4^+$  are the following dominant protonated ions (at respectively ~10% and ~3.5% for 5% injected  $\text{H}_2$ ). The improvements to the model in pure  $\text{N}_2$  thus focus on the addition of new protonated species and reactions using them as reactants or products. A particular attention is given to ammonia and surface processes (see paper II).

The variation of pressure from 0.3 to 1 mbar and coupled power from 3 to 13 W also leads to plasma modifications. An exponential increase of the electron density is observed with the increase of coupled power. It is due to the production of secondary electrons on surfaces (see paper II). On the opposite, electron density decreases with the increase of pressure.

Ammonia quantity always increases similarly to  $\text{NH}_2^+$  and  $\text{NH}_3^+$ , which suggests a strong dependence between these species,  $\text{NH}_2^+$  and  $\text{NH}_3^+$  being easily formed by direct ionization of  $\text{NH}_3$ . Ammonia absolute density stays constant with a pressure variation. Therefore, it suggests that ammonia formation is not governed only by bulk processes but mainly by surface processes. This point is discussed further in paper II. On the other hand, ions are formed in the bulk and disappear at the contact of surfaces. Their quantities are more sensitive to pressure variations. In particular,  $\text{NH}_4^+$ ,  $\text{N}_2\text{H}^+$ ,  $\text{H}_3^+$ ,  $\text{N}_3^+$ ,  $\text{N}_4^+$  and  $\text{N}_3\text{H}^+$ , which require ion-neutral gas phase reactions to form, increase at higher pressure compared to other ions formed by direct ionization (especially  $\text{N}_2^+$  and  $\text{N}^+$ ). The increase of coupled power seems to have an opposite effect by enhancing the formation of ions by direct ionization, with the increase of  $\text{N}_2^+$ ,  $\text{NH}^+$ ,  $\text{NH}_2^+$ ,  $\text{NH}_3^+$ ,  $\text{H}_2^+$  and the decrease of  $\text{NH}_4^+$ ,  $\text{N}_2\text{H}^+$  and  $\text{N}_2\text{H}_2^+$ .

On the present work we analysed new plasma conditions, different from the studies by [16,17,31,35]. Experiments were performed with only a few percent of  $\text{H}_2$  (< 5% here, compared to > 40% in the studies cited above), at lower powers (~10 W compared to > 50 W) and higher pressures (~1 mbar compared to < 0.08 mbar). All these changes lead to a lower relative production of ammonia (0.15% compared to > 3%).

The conditions used here are very similar to plasmas in planetary atmospheres. Ionization degree is varied from  $2 \cdot 10^{-8}$  to  $5 \cdot 10^{-7}$  according to the studied parameters. These values are typically similar to ionization degrees in planetary atmospheres. In particular, it corresponds to the altitude range of 950 – 1100 km on Titan, where organic aerosols form in the  $\text{N}_2\text{-CH}_4\text{-H}_2$  plasma [65]. This validates the idea of an experimental simulation of Titan's ionosphere with a RF CCP discharge [22]. The comprehension of  $\text{N}_2\text{-H}_2$  plasmas is a first step in the analysis of  $\text{N}_2\text{-CH}_4\text{-H}_2$  discharges that are chemically highly complex. In particular, [66] shows that  $\text{N}_2\text{-H}_2$  plasma species are suspected to erode organic particles also present in the ionosphere of Titan. The understanding of  $\text{N}_2\text{-H}_2$  laboratory plasmas can be very useful to understand the ion chemistry in the ionospheres of planets.

## Acknowledgements

---

N. Carrasco acknowledges the financial support of the European Research Council (ERC Starting Grant PRIMCHEM, Grant agreement no. 636829).

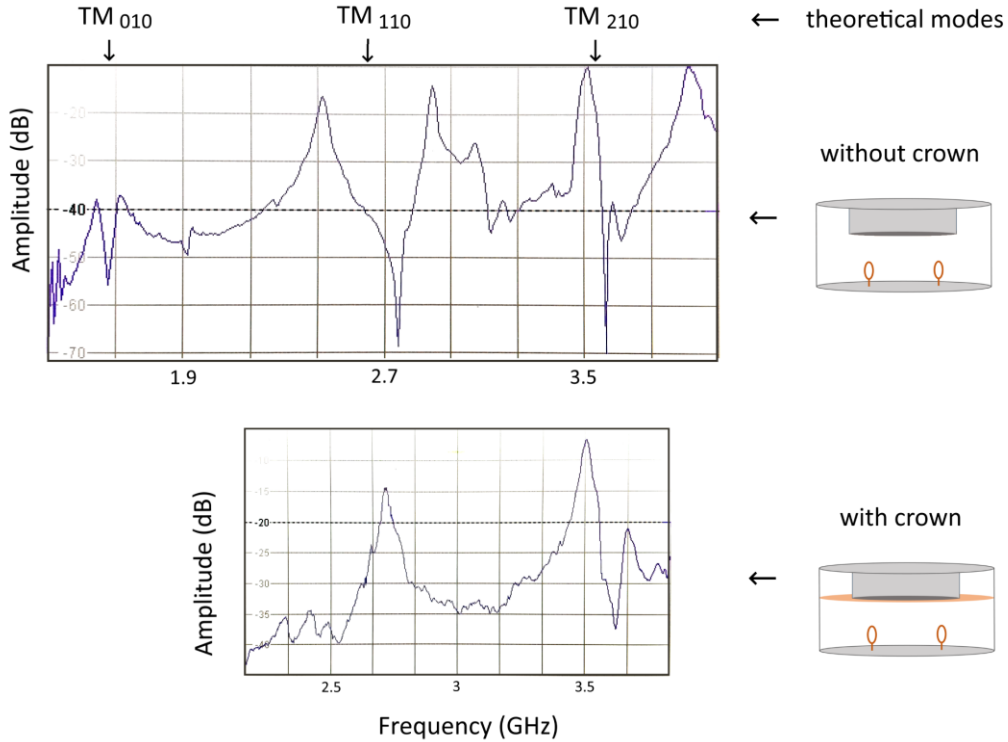
A. Chatain acknowledges ENS Paris-Saclay Doctoral Program. A. Chatain is grateful to Gilles Cartry and Thomas Gautier for fruitful discussions on the MS calibration.

L.L. Alves acknowledges the financial support of the Portuguese Foundation for Science and Technology (FCT) through the project UID/FIS/50010/2019.

L. Marques and M. J. Redondo acknowledge the financial support of the Portuguese Foundation for Science and Technology (FCT) in the framework of the Strategic Funding UIDB/04650/2019.

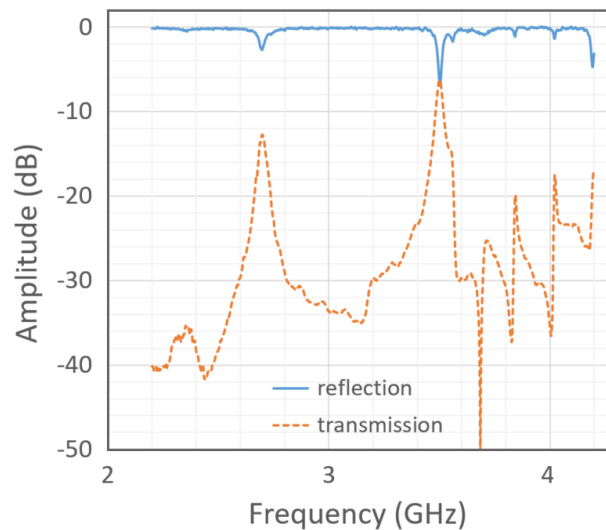
## APPENDIX A1. Improvements of the resonant cavity method

Figure A1-1 presents these resonant TM modes obtained without and with the crown. These spectra are obtained in the configuration with two antennas (transmission mode). Especially, the  $TM_{110}$  and  $TM_{210}$  are more clearly identified with the crown.



**Figure A1-1.** Spectra showing resonant TM modes in the box, without and with the copper crown.

The resonance is also detected by the reflection on the emitting antenna. Spectra acquired in transmission (with two antennas) and in reflection (with one antenna) are presented figure A1-2. The signal in reflection has a more stable baseline and thinner peaks. As the signal for the  $TM_{210}$  mode is the most intense, measurements of resonance shifts are done in reflection, and with this mode.



**Figure A1-2.** Resonances of the  $TM_{110}$   $TM_{210}$  frequencies in the box, in reflection and in transmission.

## APPENDIX A2. Calibration of MS NH<sub>3</sub> measurements by IR spectroscopy

As mentioned above in the experimental section, IR absorption measurements are very long whereas mass spectrometry measurements are faster. But mass spectrometer gives only relative values.

Ammonia is created in the confined plasma at the center of the chamber; it diffuses through the grids of the metallic box, fills all the volume of the chamber and adsorbs on the chamber's walls. Depending on the plasma conditions, it can take several hours to reach the steady state of ammonia flux, and therefore a homogeneous ammonia spatial distribution in the chamber.

The spatial homogeneity and the reaching of the steady state of ammonia density in the chamber are studied with the mass spectrometer. Its collecting head can be radially moved from the metallic box to the wall of the chamber for measurements at different locations. Figure A2-1 shows that the spatial distribution of NH<sub>3</sub> is homogeneous. For calibration measurements, the IR spectrum is integrated over ~2h, and we similarly integrate the mass spectrum over the same acquisition period.

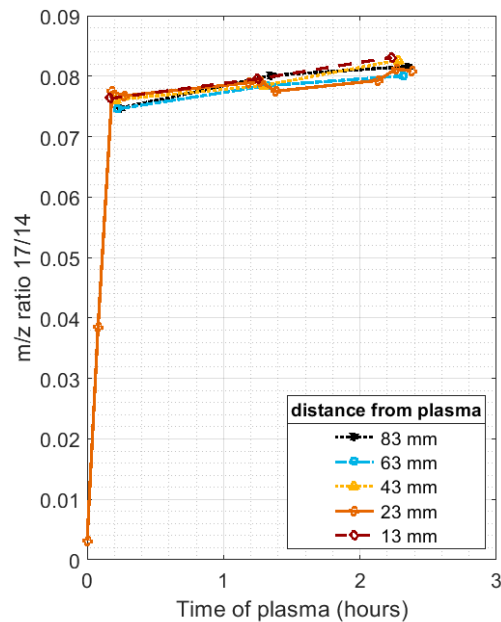


**Figure A2-1.** Variation of m/z ratio 17/14 (representative of ammonia) in time and distance from plasma (0.53 mbar – 3% H<sub>2</sub> – 8.4 W).

As NH<sub>3</sub> is homogeneous along a chamber diameter, the density can directly be deduced from the IR absorption. For a given experimental conditions, this density is compared with the ratio 17/14 of the mass spectrometer m/z intensities as presented figure A2-2.

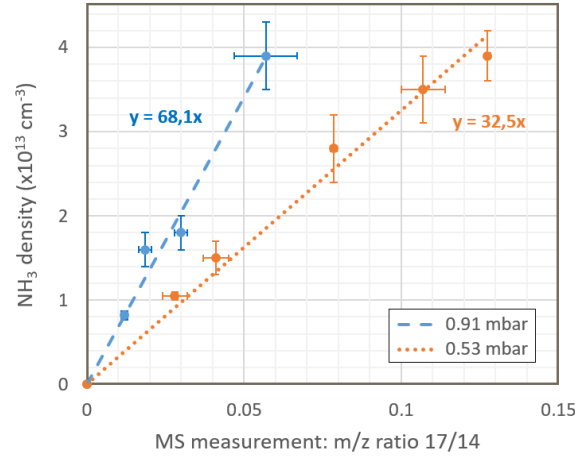


**Figure A2-2.** Calibration of MS measurements of  $\text{NH}_3$  with IR data. Experiments done at 2 different pressures (0.91 and 0.53 mbar) in a  $\text{N}_2\text{-H}_2$  plasma discharge, for a same RF peak-to-peak voltage of 480 V (at resp. 14 and 8.5 W).

The calibrations curves lead to the following calibration formula:

$$[\text{NH}_3] \approx \frac{I(17)}{I(14)} * 70 * P (. 10^{13} \text{cm}^{-3}) \quad [\text{A2.1}]$$

with  $[\text{NH}_3]$  the average ammonia density in the chamber,  $\frac{I(17)}{I(14)}$  the ratio of intensities measured at  $m/z$  17 and  $m/z$  14 by the mass spectrometer, corrected of any water contribution, and  $P$  the pressure in mbar.

### APPENDIX A3. Stabilization of MS measurements (neutrals and ions)

Neutrals and positive ions are measured continuously from the ignition of the plasma to the end of the experiment. Both measurements take some minutes to stabilize. This is mainly due to two effects: the stabilization of the species densities in the plasma and the stabilization of the MS measurement, which is likely to vary due to charging effects at the beginning of the acquisition. For the intensity measurements of neutrals and ions, the stabilization time is noted in all cases, and an average is done on the acquired signal only after the signal is stabilized.

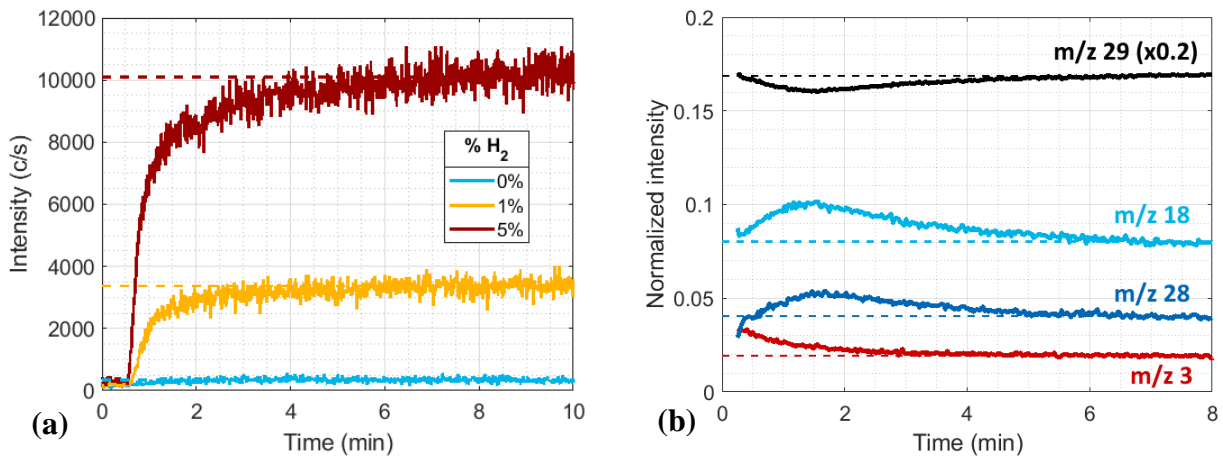


**Figure A3-1.** MS continuous acquisition in RGA and ion modes at the ignition of the plasma. (a) Intensity of  $m/z$  17 (representative of  $\text{NH}_3$  amount) at the ignition of  $\text{N}_2$  and  $\text{N}_2\text{-H}_2$  plasmas (0.53 mbar – 6.5 W). (b) Evolution of  $m/z$  3 ( $\text{H}_3^+$ ), 18 ( $\text{NH}_4^+$ ), 28 ( $\text{N}_2^+$ ) and 29 ( $\text{N}_2\text{H}^+$ ) in time until stabilization (5%  $\text{H}_2$  – 0.86 mbar – 10.5 W).

## APPENDIX A4. Transmission of the mass spectrometer as function of $m/z$

### Total transmission for different tunes

The transmission of atoms/molecules through the mass spectrometer depends on their mass, but also on the parameters of the MS. The parameters have been tuned once to optimize the intensity of  $m/z$  28 ( $N_2^+$ ), and once to optimize the intensity of  $m/z$  2 ( $H_2^+$ ). Calibration curves have been obtained for both sets of parameters and are plotted in figure A4-1. They give very different shapes, one peaked on  $m/z \sim 10$ , the other on  $m/z < 2$ .

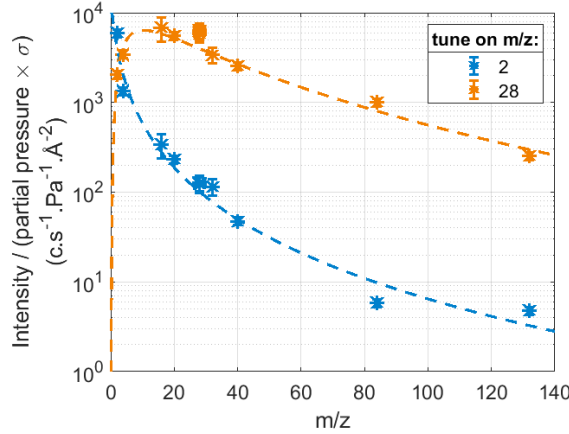


**Figure A4-1.** MS transmission as function of mass for two different sets of parameters, obtained for the optimization of the intensity of mass 2 and 28 in a  $N_2$ - $H_2$  gas mixture.

### Transmission through the pin hole aperture ( $T_{ap}$ )

To obtain the ion flux inside the MS, transmissions through the 100  $\mu m$  aperture and through the ionization chamber have to be modelled. At the entrance of the MS, the gas goes through a 100  $\mu m$  hole. The main function of this hole is to reduce the pressure inside the MS, from  $\sim 1$  mbar to  $\sim 10^{-5}$  mbar. The passage of the hole can induce a differential transmission of the atoms and molecules depending on their mass. It is governed by the flow regime, represented by the Knudsen number, ratio of the Debye length to the characteristic length of the system. The Knudsen number of the system is  $\sim 1$ . Therefore, the flow is in a transition regime between a free molecular flow regime, where gas-wall collisions dominate, and a viscous regime, where gas-gas collisions prevail. Gas flows ( $Q$ ) in the two different regimes are described in [51]:

$$Q_{molecular,X} = A \cdot \frac{v_X}{4} \cdot (P_{X,0} - P_{X,MS}) \quad \text{with } v_X = \sqrt{\frac{8 \cdot k_B T}{\pi \cdot m_X}} \quad [A4.1]$$

$$Q_{viscous,X} = A \cdot P_{X,0} \cdot \sqrt{k_B T} \cdot C_2 \times \frac{1}{\sqrt{m_{avg}}} \quad \text{with } C_2 = C' \times \sqrt{\frac{2\gamma}{\gamma+1}} \times \left(\frac{2}{\gamma+1}\right)^{\frac{\gamma}{\gamma-1}} \quad [A4.2]$$

$$\text{with the respected condition for [A4.2]: } \sim 10^{-5} = \frac{P_{MS}}{P_0} \leq \left(\frac{2}{\gamma+1}\right)^{\frac{\gamma}{\gamma-1}} \approx 0.5$$

$A$  is the surface area of the hole.  $v_x$  and  $m_x$  are the velocity and the mass of the atom / molecule  $X$ .  $P_{x,0}$  and  $P_{x,MS}$  are the partial pressures of  $X$  respectively in the reactor chamber and in the MS, with  $P_{x,MS} \ll P_{x,0}$ .  $k_B$  is the Boltzmann constant and  $T$  the gas temperature (supposed constant).  $m_{avg}$  is the average particle mass of the gas mixture injected.  $C'$  is a factor taking into account that high-speed gas stream continues to decrease in diameter after passing through the orifice. For thin circular orifices,  $C'$  is equal to  $\sim 0.85$ .  $\gamma$  is the specific heat ratio, equals to  $\sim 1.4$  for diatomic gases, 1.667 for monoatomic gases.

The transition regime is more complex to define. [51] and [52] consider a linear combination of  $Q_{\text{molecular},x}$  and  $Q_{\text{viscous},x}$ , with a coefficient depending on the Knudsen number:

$$Q_{\text{transition},X} = Q_{\text{viscous},X} + Z \times Q_{\text{molecular},X} \quad \text{with } Z \approx \frac{1}{1 + \frac{3\pi}{128} \frac{1}{Kn}} \quad [\text{A4.3}]$$

On the other hand, the gas flow can be expressed as a function of the pumping speed ( $S_p$ ) and the MS pressure [53]:

$$Q_X = P_{MS,X} \times S_p \quad [\text{A4.4}]$$

From equations [A4.1], [A4.2], [A4.3] and [A4.4], we can deduce the transmission through the 100  $\mu\text{m}$  aperture:

$$T_{ap}(m_X) \equiv \frac{P_{X,MS}}{P_{X,0}} \approx \frac{A}{S_p} \cdot \sqrt{k_B T} \times \left( \frac{C_{\text{visc}}}{\sqrt{m_{\text{avg}}}} + \frac{Z}{\sqrt{2\pi \cdot m_X}} \right) \propto \frac{C_{\text{visc}}}{\sqrt{m_{\text{avg}}}} + \frac{0.38}{\sqrt{m_X}} \quad [\text{A4.5}]$$

with  $C_{\text{visc}} = 0.46$  for atoms and  $C_{\text{visc}} = 0.49$  for diatomic molecules and methane.

### Transmission through the ionization chamber ( $T_{\text{ioni}}$ )

The transmission through the ionization chamber links the neutral density of the atom / molecule X entering the chamber ( $n_{x,MS}$ ) to the ion flux inside the MS ( $j_{x+,MS}$ ). They are linked by the simple ionization cross section ( $\sigma_x$ ).

$$\frac{dn_X}{dt} = -\sigma_X n_X n_e v_e \quad \Rightarrow \quad n_X(t) = n_{X,MS} \times \exp(-\sigma_X n_e v_e t) \quad \text{with } t = \frac{L}{v_X} \quad [\text{A4.6}]$$

for t corresponding to the crossing of the ionization chamber by X. L is the length of the ionization chamber,  $n_x$  (resp.  $n_e$ ) the density of X (resp. electrons) in the ionization chamber,  $v_x$  (resp.  $v_e$ ) the velocity of X (resp. electrons). As  $\frac{\sigma_X n_e v_e L}{v_X} \sim 10^{-7} \ll 1$ , the Taylor expansion gives:

$$n_{X,L} \approx n_{X,MS} \times \left( 1 - \frac{\sigma_X n_e v_e L}{v_X} \right) \quad [\text{A4.7}]$$

The evolution of X density is directly linked to the formation of the ion  $X^+$ .

$$n_{X^+,L} = n_{X,MS} - n_{X,L} = n_{X,MS} \times \left( \frac{\sigma_X n_e v_e L}{v_X} \right) \quad [\text{A4.8}]$$

Ion flux ( $j_{X^+,MS}$ , in  $\text{s}^{-1} \cdot \text{m}^{-2}$ ) and electron current ( $I_e$ , in A) are more convenient to use than ion and electron densities in the ionization chamber.

$$j_{X^+,MS} = \frac{1}{4} n_{X^+,L} \times v_{X^+} \quad [\text{A4.9}]$$

$$I_e = \frac{1}{4} n_e \times v_e \times e \times l \times L \quad [\text{A4.10}]$$

with  $v_{X^+}$  the velocity of the ion  $X^+$ , supposed equal to  $v_x$  in the ionization chamber, e the elementary charge, l the width and L the length of the ionization chamber.

The relation between  $j_{X^+}$  and  $n_{X,MS}$  is obtained by combining [A4.8], [A4.9] and [A4.10]:

$$j_{X^+} = n_{X,MS} \times \sigma_X \times \frac{I_e}{l.e} = n_{X,MS} \times T_{ioni}(X) \quad \text{with} \quad T_{ioni}(X) \equiv \sigma_X \times \frac{I_e}{l.e} = \sigma_X \times cst$$

The only dependence in the atom/molecule X chosen is the simple ionization cross section ( $\sigma_X$ ).  $T_{ioni}$  has *a priori* no dependence in mass.

### Energy scans of ions

To compare intensities measured for different ions on a same spectrum, one should check these ions have similar energy distributions, with the same maximum. This comparison has been done on  $N_2$ - $H_2$  plasma ions. For absolute values of the extractor below  $\sim 60$  V, and  $m/z$  above  $\sim 10$ , this condition is valid (see figure A4-2).

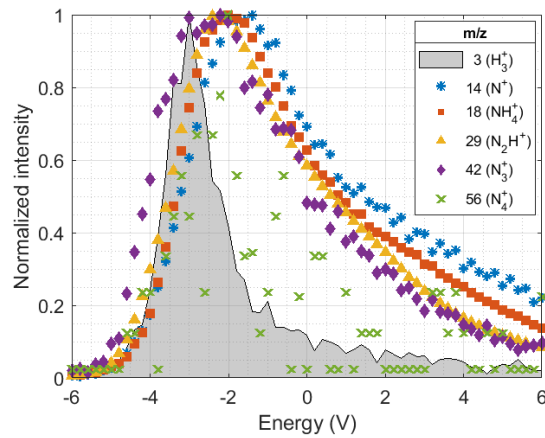


**Figure A4-2.** Energy scans for different ions in a  $N_2$ - $H_2$  plasma at 0.80 mbar. The extractor was fixed to -40 V. Note: the reference of energy axis is not calibrated and is certainly shifted of a few volts.

## References

---

- [1] Cernogora G, Hochard L, Touzeau M and Matos Ferreira C 1981 Population of N<sub>2</sub>(A 3Σ<sup>u</sup>+) metastable states in a pure nitrogen glow discharge *J. Phys. B At. Mol. Phys.* **14** 2977–87
- [2] Guerra V, Sá P A and Loureiro J 2004 Kinetic modeling of low-pressure nitrogen discharges and post-discharges *EPJ Appl. Phys.* **28** 125–52
- [3] Shirley J A and Hall R J 1977 Vibrational excitation in H<sub>2</sub> and D<sub>2</sub> electric discharges *J. Chem. Phys.* **67** 2419–21
- [4] Amorim J, Loureiro J and Schram D 2001 Formation of H<sup>-</sup> ions via vibrational excited molecules produced from recombinative wall desorption of H atoms in a low-pressure H<sub>2</sub> positive column *Chem. Phys. Lett.* **346** 443–8
- [5] Watanabe H, Katoh K and Imagi S-I 1986 Properties of silicon nitride films prepared by plasma-enhanced chemical vapour deposition of SiH<sub>4</sub>-N<sub>2</sub> mixtures *Thin Solid Films* **136** 77–83
- [6] Sekine K, Saito Y, Hirayama M and Ohmi T 1999 Silicon nitride film growth for advanced gate dielectric at low temperature employing high-density and low-energy ion bombardment *J. Vac. Sci. Technol. A Vacuum, Surfaces, Film.* **17** 3129–33
- [7] Aberle A G 2001 Overview on SiN surface passivation of crystalline silicon solar cells *Sol. Energy Mater. Sol. Cells* **65** 239–48
- [8] Wróbel A M, Błaszczuk I, Walkiewicz-Pietrzykowska A, Tracz A, Klemberg-Sapieha J E, Aoki T and Hatanaka Y 2003 Remote hydrogen-nitrogen plasma chemical vapor deposition from a tetramethyldisilazane source. Part 1. Mechanism of the process, structure and surface morphology of deposited amorphous hydrogenated silicon carbonitride films *J. Mater. Chem.* **13** 731–7
- [9] Hudis M 1973 Study of ion-nitriding *J. Appl. Phys.* **44** 1489–96
- [10] Bouanis F Z, Jama C, Traisnel M and Bentiss F 2010 Study of corrosion resistance properties of nitrided carbon steel using radiofrequency N<sub>2</sub>/H<sub>2</sub> cold plasma process *Corros. Sci.* **52** 3180–90
- [11] Tabarés F L, Tafalla D, Tanarro I, Herrero V J, Islyaikin A, Maffiotte C, Tabarés F L, Tafalla D, Tanarro I, Herrero V J, Islyaikin A and Maffiotte C 2002 Suppression of hydrogenated carbon film deposition by scavenger techniques and their application to the tritium inventory control of fusion devices *Plasma Phys. Control. Fusion* **44** L37–42
- [12] Oberkofler M, Alegre D, Aumayr F, Brezinsek S, Dittmar T, Dobes K, Douai D, Drenik A, Köppen M, Kruezi U, Linsmeier C, Lungu C P P, Meisl G, Mozetic M, Porosnicu C, Rohde V and Romanelli S G G 2015 Plasma-wall interactions with nitrogen seeding in all-metal fusion devices: Formation of nitrides and ammonia. *Fusion Eng. Des.* **98–99** 1371–4
- [13] Body T, Cousens S, Kirby J and Corr C 2018 A volume-averaged model of nitrogen-hydrogen plasma chemistry to investigate ammonia production in a plasma-surface-interaction device *Plasma Phys. Control. Fusion* **60**
- [14] Hong J, Pancheshnyi S, Tam E, Lowke J J, Prawer S and Murphy A B 2017 Kinetic modelling of NH<sub>3</sub> production in N<sub>2</sub>-H<sub>2</sub> non-equilibrium atmospheric-pressure plasma catalysis *J. Phys. D. Appl. Phys.* **50**
- [15] Wang H-X, Geng J-Y, Chen X, Pan W X and Murphy A B 2010 Modeling Study on the Flow, Heat Transfer and Energy Conversion Characteristics of Low-Power Arc-Heated Hydrogen/Nitrogen Thrusters *Plasma Chem. Plasma Process.* **30** 707–31
- [16] Carrasco E, Jiménez-Redondo M, Tanarro I and Herrero V J 2012 Chemistry in low-pressure cold plasmas: Ions of astrophysical interest *Plasma Phys. Control. Fusion* **54**
- [17] Carrasco E, Tanarro I, Herrero V J and Cernicharo J 2013 Proton transfer chains in cold plasmas of H<sub>2</sub> with small amounts of N<sub>2</sub>. The prevalence of NH<sub>4</sub><sup>+</sup>. *Phys. Chem. Chem. Phys.* **15** 1699–706
- [18] Herbst E 2001 The chemistry of interstellar space *Chem. Soc. Rev.* **30** 168–76
- [19] Petrie S and Bohme D K 2007 Ions in space *Mass Spectrom. Rev.* **26** 258–80
- [20] Womack M, Ziurys L M and Wyckoff S 1992 A survey of N<sub>2</sub>H<sup>+</sup> in dense clouds - Implications for interstellar nitrogen and ion-molecule chemistry *Astrophys. J.* **387** 417
- [21] Cui J, Yelle R V., Vuitton V, Waite J H, Kasprzak W T, Gell D A, Niemann H B, Müller-Wodarg I C F, Borggren N, Fletcher G G, Patrick E L, Raaen E and Magee B A 2009 Analysis of Titan's neutral upper atmosphere from Cassini Ion Neutral Mass Spectrometer measurements *Icarus* **200** 581–615
- [22] Szopa C, Cernogora G, Boufendi L, Correia J J and Coll P 2006 PAMPRE: A dusty plasma experiment for Titan's tholins production and study *Planet. Space Sci.* **54** 394–404

- [23] Sciamma-O'Brien E, Ricketts C L, Salama F and Sciamma-O'Brien E 2014 The titan haze simulation experiment on cOsmic: Probing titan's atmospheric chemistry at low temperature *Icarus* **243** 325–36
- [24] Coll P, Coscia D, Smith N, Gazeau M C, Ramírez S I, Cernogora G, Israël G and Raulin F 1999 Experimental laboratory simulation of Titan's atmosphere: Aerosols and gas phase *Planet. Space Sci.* **47** 1331–40
- [25] Yelle R V., Vuitton V, Lavvas P, Klippenstein S J, Smith M A, Hörst S M and Cui J 2010 Formation of NH<sub>3</sub> and CH<sub>2</sub>NH in Titan's upper atmosphere *Faraday Discuss.* **147**
- [26] Dobrijevic M, Loison J C, Hickson K M and Gronoff G 2016 1D-coupled photochemical model of neutrals, cations and anions in the atmosphere of Titan *Icarus* **268** 313–39
- [27] Loureiro J and Ricard A 1993 Electron and vibrational kinetics in an N<sub>2</sub>-H<sub>2</sub> glow discharge with application to surface processes *J. Phys. D. Appl. Phys.* **26** 163–76
- [28] Garscadden A and Nagpal R 1995 Non-equilibrium electronic and vibrational kinetics in H<sub>2</sub>-N<sub>2</sub> and H<sub>2</sub> discharges *Plasma Sources Sci. Technol.* **4** 268–80
- [29] Gordiets B, Ferreira C M, Pinheiro M J and Ricard A 1998 Self-consistent kinetic model of low-pressure N<sub>2</sub>-H<sub>2</sub> flowing discharges: I. Volume processes *Plasma Sources Sci. Technol.* **7** 363–78
- [30] Gordiets B, Ferreira C M, Pinheiro M J and Ricard A 1998 Self-consistent kinetic model of low-pressure N<sub>2</sub>-H<sub>2</sub> flowing discharges: II. Surface processes and densities of N, H, NH<sub>3</sub> species *Plasma Sources Sci. Technol.* **7** 379–88
- [31] Carrasco E, Jiménez-Redondo M, Tanarro I and Herrero V J 2011 Neutral and ion chemistry in low pressure dc plasmas of H<sub>2</sub>/N<sub>2</sub> mixtures: Routes for the efficient production of NH<sub>3</sub> and NH<sub>4</sub><sup>+</sup> *Phys. Chem. Chem. Phys.* **13** 19561–72
- [32] Hong J, Pancheshnyi S, Tam E, Lowke J J, Prawer S and Murphy A B 2018 Erratum: Kinetic modelling of NH<sub>3</sub> production in N<sub>2</sub>-H<sub>2</sub> non-equilibrium atmospheric-pressure plasma catalysis *J. Phys. D. Appl. Phys.* **51**
- [33] Leyland A, Fancey K S, James A S and Matthews A 1990 Enhanced plasma nitriding at low pressures: A comparative study of d.c. and r.f. techniques *Surf. Coatings Technol.* **41** 295–304
- [34] Tatarova E, Dias F M, Gordiets B and Ferreira C M 2005 Molecular dissociation in N<sub>2</sub>-H<sub>2</sub> microwave discharges *Plasma Sources Sci. Technol.* **14** 19–31
- [35] Sode M, Jacob W, Schwarz-Selinger T and Kersten H 2015 Measurement and modeling of neutral, radical, and ion densities in H<sub>2</sub>-N<sub>2</sub>-Ar plasmas *J. Appl. Phys.* **117** 083303
- [36] Salabas A, Marques L, Jolly J, Gousset G and Alves L L 2004 Systematic characterization of low-pressure capacitively coupled hydrogen discharges *J. Appl. Phys.* **95** 4605–20
- [37] Marques L, Jolly J and Alves L L 2007 Capacitively coupled radio-frequency hydrogen discharges: The role of kinetics *J. Appl. Phys.* **102**
- [38] Alves L L, Marques L, Pintassilgo C D, Wattieaux G, Es-Sebbar E, Berndt J, Kovacević E, Carrasco N, Boufendi L and Cernogora G 2012 Capacitively coupled radio-frequency discharges in nitrogen at low pressures *Plasma Sources Sci. Technol.* **21** 045008
- [39] Alcouffe G, Cavarroc M, Cernogora G, Ouni F, Jolly A, Boufendi L and Szopa C 2010 Capacitively coupled plasma used to simulate Titan's atmospheric chemistry *Plasma Sources Sci. Technol.* **19** 015008
- [40] Annemie, Bogaerts, Neyts E, Gijbels R and Mullen J Van der 2002 Gas Discharge Plasmas and Their Applications *Spectrochim. Acta Part B* **57** 609–58
- [41] Wattieaux G, Carrasco N, Henault M, Boufendi L and Cernogora G 2015 Transient phenomena during dust formation in a N<sub>2</sub>-CH<sub>4</sub> capacitively coupled plasma *Plasma Sources Sci. Technol.* **24** 015028
- [42] Haverlag M, Kroesen G M W, Bisschops T H J and de Hoog F J 1991 Measurement of electron densities by a microwave cavity method in 13.56-MHz RF plasmas of Ar, CF<sub>4</sub>, C<sub>2</sub>F<sub>6</sub>, and CHF<sub>3</sub> *Plasma Chem. Plasma Process.* **11** 357–70
- [43] Gautier T, Carrasco N, Buch A, Szopa C, Sciamma-O'Brien E and Cernogora G 2011 Nitrile gas chemistry in Titan atmosphere *Icarus* **213** 625
- [44] Dubois D, Carrasco N, Petrucciani M, Vettier L, Tigrine S and Pernot P 2019 In situ investigation of neutrals involved in the formation of Titan tholins *Icarus* **317** 182–96
- [45] Klarenaar B L M, Engeln R, Van Den Bekerom D C M, Van De Sanden M C M, Morillo-Candas A S and Guaitella O 2017 Time evolution of vibrational temperatures in a CO<sub>2</sub> glow discharge measured with infrared absorption spectroscopy *Plasma Sources Sci. Technol.* **26** 115008
- [46] Kechkar S, Babu S K, Swift P, Gaman C, Daniels S and Turner M 2014 Investigation of absolute atomic fluorine density in a capacitively coupled SF<sub>6</sub>/O<sub>2</sub>/Ar and SF<sub>6</sub>/Ar discharge *Plasma Sources Sci.*

- Technol.* **23** 065029
- [47] Lopaev D V, Volynets A V, Zyryanov S M, Zotovich A I and Rakhimov A T 2017 Actinometry of O, N and F atoms *J. Phys. D. Appl. Phys.* **50** 075202
- [48] Kondo Y, Ishikawa K, Hayashi T, Sekine M and Hori M 2018 Electron impact ionization of perfluoromethyl-vinyl-ether C<sub>3</sub>F<sub>6</sub>O *Plasma Sources Sci. Technol.* **27** 015009
- [49] Sode M, Schwarz-Selinger T and Jacob W 2013 Quantitative determination of mass-resolved ion densities in H<sub>2</sub>-Ar inductively coupled radio frequency plasmas *J. Appl. Phys.* **113**
- [50] Pulpytel J, Arefi-Khonsari F and Morscheidt W 2005 Threshold ionization mass spectrometry study of singlet molecular oxygen in the deposition of SnO<sub>2</sub> by PACVD *J. Phys. D. Appl. Phys.* **38** 1390–5
- [51] O’Hanlon J 2003 A User’s Guide to Vacuum Technology. *Wiley, New Jersey*
- [52] Livesey R G 2001 Method for calculation of gas flow in the whole pressure regime through ducts of any length *J. Vac. Sci. Technol. A Vacuum, Surfaces, Film.* **19** 1674–8
- [53] Godet L 2006 Development of pulsed plasma doping system for semiconductor processing : characterization of the plasma and its interaction with the materials . *PhD thesis, Univ. Nantes, Fr.*
- [54] Anon Biagi Database [www.lxcat.net/Biagi](http://www.lxcat.net/Biagi)
- [55] Alves L L 2014 The IST-LISBON database on LXCat *Journal of Physics: Conference Series* vol 565
- [56] Anon IST Database [www.lxcat.net/IST-Lisbon](http://www.lxcat.net/IST-Lisbon)
- [57] Anon Phelps Database [www.lxcat.net/Phelps](http://www.lxcat.net/Phelps)
- [58] Rapp D and Englander-Golden P 1965 Total Cross Sections for Ionization and Attachment in Gases by Electron Impact. I. Positive Ionization *J. Chem. Phys.* **43** 1464–79
- [59] Isola L M, Gómez B J and Guerra V 2010 Determination of the electron temperature and density in the negative glow of a nitrogen pulsed discharge using optical emission spectroscopy *J. Phys. D. Appl. Phys.* **43** 015202
- [60] Tachibana K and Phelps A V. 1987 Excitation of the 1s<sub>5</sub> and 1s<sub>4</sub> levels of neon by low-energy electrons *Phys. Rev. A* **36** 999–1007
- [61] Yamabe C, Buckman S J and Phelps A V. 1983 Measurement of free-free emission from low-energy-electron collisions with Ar *Phys. Rev. A* **27** 1345–52
- [62] Lawton S A and Phelps A V. 1978 Excitation of the b 1Σ<sup>+</sup>+g state of O<sub>2</sub> by low energy electrons *J. Chem. Phys.* **69** 1055
- [63] Achkasov K 2015 Study of negative ion surface production in cesium-free H<sub>2</sub> and D<sub>2</sub> plasmas: application to neutral beam injectors for ITER and DEMO *PhD thesis, Univ. d’Aix-Marseille, Fr.*
- [64] Lieberman M A and Lichtenberg A J 2005 *Principles of Plasma Discharges and Materials Processing: Second Edition*
- [65] Waite J H, Young D T, Cravens T E, Coates A J, Crary F J, Magee B and Westlake J 2007 Planetary science: The process of tholin formation in Titan’s upper atmosphere *Science (80-. )*. **316** 870–5
- [66] Chatain A, Carrasco N, Ruscassier N, Gautier T, Vettier L and Guaitella O 2020 Interaction dust – plasma in Titan’s ionosphere: an experimental simulation of aerosols erosion *Submitt. to Icarus*